

Eruptive dynamics and fragmentation mechanisms during cyclic Vulcanian activity at Sakurajima volcano (Japan): insights from ash texture analysis

Pietro Gabellini¹, Raffaello Cioni¹, Nobuo Geshi², Marco Pistolesi³, Takahiro Miwa⁴, Giorgio Lacanna¹, Maurizio Ripepe¹

¹ Dip.to Scienze della Terra, Florence, Italy

² National Research Institute for Earth Science and Disaster Resilience, Tsukuba, Japan

³ Dip.to Scienze della Terra, Pisa, Italy

⁴ Geological Survey of Japan, AIST, Tsukuba, Japan

Abstract

Quantitative morpho-textural analysis of volcanic ash is one of the most effective tools to characterize the style of ash-dominated volcanic activity, and to investigate the complex interplay between conduit processes and the associated eruptive dynamics. In this framework, many questions still remain unanswered about the role of conduit processes, particularly of the magma fragmentation processes, in controlling the eruptive dynamics of the unsteady and highly-transient Vulcanian explosions. For this reason, we analyzed ash samples collected during a five days-long eruptive sequence at Sakurajima volcano (Japan), to derive information about ash morphometry and textural features over the entire sequence. During the observed sequence, eruptive activity showed high unsteadiness in the modalities of ash emission, which included all the main different eruptive styles typical of the recent period of Sakurajima activity. Three main intra-eruptive phases (Phase1, Phase2 and Phase3) were recognized based on visual observations and thermal data. Quantitative information about external ash morphometry (i.e., shape) and internal textures were measured for the particles associated with the different phases and discussed in terms of the observed eruptive variability. We quantified crystallinity and vesicularity of ash grains, the crystal size distribution (CSD) of microlites and the microlite number density (MND) of the groundmass for a representative set of ash particles. We discussed the links between the eruptive dynamics and the dominant processes of magma fragmentation, as shown by the combination of the morpho-textural features of ash throughout the whole eruptive sequence and the observed variations of the eruptive phases. All the evidence presented in this work confirm the constant presence at Sakurajima of a highly stratified and degassed magma within the conduit, suggesting that the transient dynamics of the eruption were strongly controlled by variations in the process of magma fragmentation driving the eruptions during the different phases. In particular, the morpho-textural

characteristics of ash suggest that Vulcanian eruptions at Sakurajima can be controlled by the progressive pressurization of the upper portion of the magma conduit (between 10 and 50 m in depth). Moreover, using crystal textures, we inferred that the time needed for conduit refilling during intra-eruptive stages is comprised between 1 and 10 month. The resulting information on the eruptive dynamics of Sakurajima is of primary importance for a more exhaustive comprehension of the low-to-mid intensity, ash-dominated explosive activities.

1. Introduction

Large amounts of volcanic ash are frequently produced during low- to mid-intensity explosive eruptions at many active volcanoes worldwide (e.g. [Heiken and Wohletz, 1985](#); [Sparks et al., 1997](#); [Dingwell et al., 2012](#); [Mackie et al., 2016](#); [Bernard et al., 2016](#); [Oishi et al., 2018](#); [Battaglia et al., 2019](#)). The sudden ash discharge related to explosive eruptions often represents a critical source of hazard for the population living near active volcanoes, and for the civil aviation ([Casadevall and Krohn, 1995](#); [Sparks et al., 1997](#); [Guffanti et al., 2010](#)). Despite the high frequency of ash-dominated activity at the global scale, and the consequent relevant societal impact, the mechanisms responsible for ash generation and dispersal during these eruptions are still not fully understood. On the other hand, volcanic ash is widely recognized to represent a powerful tool for the investigation of the eruptive dynamics and of all the processes affecting magma during its upward migration in the conduit (e.g. [Taddeucci et al., 2004](#); [Wright et al., 2012](#); [Cioni et al., 2014](#)). The scientific community spent many efforts to improve the knowledge about physical processes responsible for ash generation, transport and dispersal (e.g. [Dellino and La Volpe, 1996](#); [Cioni et al., 2008](#); [Miwa and Geshi, 2012](#); [Cioni et al., 2014](#); [Bonadonna et al., 2015](#); [Cashman and Scheu, 2015](#); [Liu et al., 2015](#); [Liu et al., 2017](#); [Durant, 2015](#); [Hantusch et al., 2021](#)). Since the pioneering work of [Heiken and Wohletz \(1985\)](#), who firstly provided a comparative study of ash textures and morphological features over various types of eruptive styles, several studies have been later focused on volcanic ash to investigate in detail both conduit and eruptive processes, and to make inferences on the nature of magma fragmentation mechanisms ([Büttner et al., 1999](#); [Alidibirov and Dingwell, 2000](#); [Cashman et al., 2008](#); [Miwa et al., 2013](#); [Cioni et al., 2014](#); [Jordan et al., 2014](#); [Leibrandt and Le Pennec, 2015](#); [Mackie et al., 2016](#); [Battaglia et al., 2019](#)). Quantifying the physical features (e.g. vesicularity, crystallinity, external and surface morphology) of volcanic ash resulted in better constraints for the mechanisms of magma fragmentation, and informed about their role in influencing the eruptive dynamics ([Cashman, 1992](#); [Cashman and Hoblitt, 2004](#); [Alidibirov and Dingwell, 2000](#); [Wright et al., 2012](#); [Miwa and Toramaru, 2013](#); [Miwa et al., 2013](#); [Cioni et al., 2014](#); [Cashman and Scheu, 2015](#); [Gaunt et al., 2016](#); [Liu et al., 2017](#)). Importantly, information on the internal texture of ash was also used to better understand and interpret the highly unsteady (i.e. transitory) behavior often observed in the dynamics of mid-intensity and high-frequency explosive eruptions ([Miwa et al., 2009](#); [Cashman et al., 2008](#); [Miwa and Toramaru, 2013](#); [Miwa et al., 2013](#); [Cioni et al., 2014](#)). As a matter of fact, while a lot of

work has been done for the comprehension of sustained volcanic activity (e.g. Plinian eruptions), several questions still remain unsolved about the role that mechanisms of magma fragmentation have in the control of the intra-eruptive variability in the intensity and style often observed during low- to mid-intensity, ash-dominated eruptions (e.g. Vulcanian-like activity).

Here we present the results of a study designed to quantitatively characterize the texture of the ash produced during the most recent (post 1955), highly-transient activity of Sakurajima volcano (Japan). Ash was directly collected during a five-days eruptive sequence that occurred during October 2014 characterized by repeated (from seconds to hours) transitions in intensity and style of the activity. At least three different phases of activity were identified, encompassing a large spectrum of intensity. This feature makes the collected samples particularly valuable for investigating the mechanisms responsible for the important variations observed in the eruptive dynamics. We quantified the main physical characteristics (grain-size, morphology, crystallinity and texture) of ash products related to the different eruptive stages, discussing the results in the light of conduit dynamics. We finally made inferences on the nature of magma fragmentation processes during the different stages of the activity.

All the collected data suggest the constant presence at Sakurajima of a highly stratified and degassed magma plug at the top of the conduit. This led us to interpret the unsteady dynamics of the observed eruption as related to a variable process of magma fragmentation mainly driven by the progressive pressure accumulation produced by gas transfer into the plug, without an important pre-eruptive magma ascent. Detailed analyses (e.g. crystallinity, vesicularity and grain-size distribution of microlites) on the ash fragments also allowed us to reconstruct the internal structure of the upper volcanic conduit and to estimate the volumetric contribution of the different portions of the plug in the process of ash production.

1.1. The recent Vulcanian activity at Sakurajima volcano

Sakurajima is an andesitic stratovolcano located in the Kagoshima prefecture (southern Kyushu, Japan; [Fig. 1a](#)) well known for the high-frequency, nearly continuous Vulcanian eruptions which characterize the volcano activity since 1955 ([Miwa et al., 2013](#); [Iguchi et al., 2008](#)). The stratovolcano is formed by two overlapping cones, Kitadake, which ended its activity at 4850 ka, and the presently active Minamidake ([Takahashi et al., 2013](#)). Since 1955, the activity occurred mainly at Minamidake summit crater, with no significant change in the chemical composition of the erupted products ([Matsumoto et al., 2013](#); [Kurniawan et al., 2016](#)). However, during June 2006, major changes in the activity occurred, marked by the shift of the activity to the parasitic Showa crater and the corresponding deactivation of Minamidake crater ([Iguchi, 2013](#)). In August 2015, activity interrupted for several months until February 2016, when it restarted first from Showa crater, with small explosive events, and then (March 2016) from Minamidake crater, with high intensity explosions (Japan Meteorological Agency, JMA; <http://www.jma.go.jp/jma/indexe.html>). Since 2016, activity alternated between the two vents, with variable energy, intensity and frequency. As reported by the JMA, Vulcanian activity of Sakurajima

is still ongoing and it consists of sequences of small tephra emissions often culminating in strong Vulcanian explosions, eventually separated by a short period during which no ash emission is observed ([Oba et al., 1980](#); [Ishihara, 2000](#); [Yamanoi et al., 2008](#); [Iguchi et al., 2008](#); [Iguchi, 2013](#); [Miwa and Toramaru, 2013](#)). A recurrent eruptive pattern in the recent activity of Sakurajima has been recognized, including different eruptive styles characterized by a range of intensity and modalities of products emission (e.g. [Kamo, 1978](#); [Fukuyama, 1981](#); [Ishihara, 1990](#); [Yamanoi et al., 2008](#); [Iguchi et al., 2008](#); [Iguchi et al., 2013](#); [Miwa et al., 2013](#)). Monitored variations in the dynamics of the volcanic activity, coupled to recorded ground deformations and other geophysical data, allowed to quantitatively characterize the typical eruptive pattern ([Iguchi et al., 2008](#); [Iguchi, 2013](#); [Yokoo et al., 2013](#)). Normally, an eruptive cycle starts with the migration of andesitic magma that accumulates in a shallow reservoir, as testified by the distribution of volcano-tectonic hypocenters and by the volcanic edifice inflation which precedes, from hours to several days, the onset of an eruption ([Ishihara, 1990](#); [Iguchi et al., 2008](#); [Iguchi et al., 2013](#); [Yokoo et al., 2013](#)). For those eruptions occurring at Showa crater, [Yokoo et al. \(2013\)](#) identified the depth of magma accumulation to be comprised between 0 and 2 km beneath the crater, at a level considerably shallower respect to the 2 to 6 km deep magma reservoir previously identified by [Ishihara \(1990\)](#). During this stage, the eruptive activity is typically marked by the onset of a low-intensity, intermittent activity characterized by phases of no-to-weak ash and gas emissions, punctuated by small explosions associated with the ejection of ballistic bombs and lapilli (e.g. [Miwa and Toramaru, 2013](#)). This phase can last from hours to days. An increasing trend of upward inflation (0.01 to 0.2 μ rad) starts from minutes to several hours (~ 20 h) before the onset of the major explosion, which is also marked by a downward and contractive signal immediately before (seconds) and after the eruption ([Iguchi et al., 2013](#); [Iguchi, 2013](#); [Yokoo et al., 2013](#)). At the same time, a decrease in SO₂ discharge rate is recorded, together with a progressive weakening of the nighttime glowing ([Yokoo et al., 2013](#)). These evidences have been interpreted by [Ishihara \(1985\)](#) and [Yokoo et al. \(2013\)](#) as due to the progressive formation of a degassed and viscous magma plug sealing the upper part of the volcanic conduit prior to the occurrence of a Vulcanian explosion. Aerial photos and textural data on ash reported by [Miwa et al. \(2013\)](#) agree in indicating the presence of a viscous and outgassed plug in the upper conduit of Sakurajima. Typically, a Vulcanian explosion occurs after a variable period of quiescence or very weak intermittent activity, as the magma column achieves sufficient pressure to overcome the lithostatic strength of the plug ([Tameguri et al., 2002](#)). Large Vulcanian explosion are typically associated to the production of variably ash-laden plumes that can reach several kilometers in the atmosphere (up to 5–6 km during stronger events). During the largest events, meter- to cm-sized ballistic fragments are often ejected up to a few km far from the vent ([Iguchi et al., 2008](#)). These events are also accompanied by violent air-shocks (exceeding 500 Pa at 2.7 km from the vent) that commonly precede the formation of convective, ash-rich plumes ([Iguchi et al., 2008](#)). [Miwa and Toramaru \(2013\)](#) interpreted the intensity of the produced air shocks as related to the amount of gas accumulated in the magma conduit before

eruptions. Immediately after strong Vulcanian explosions, it is frequent to observe a phase of continuous ash venting, accompanied by a persistent tremor without any visible associated explosion. This activity typically lasts from minutes to hours and it is characterized by the quasi-sustained emission of gas and tephra to form a weak, dense, low-level ash plume rising from the vent ([Kamo and Ishihara, 1989](#); [Nogami et al., 2006](#); [Yamanoi et al., 2008](#); [Iguchi et al., 2008](#); [Iguchi et al., 2013](#); [Miwa et al., 2013](#)). Typically, the ash emission ceases with the gradual decrease in frequency and intensity of the seismic signals ([Iguchi et al., 2008](#)). Then, a variable period lasting from hours to days of no visible activity commonly precedes a low-level ash or gas emission, which corresponds with the start of a new cycle. While the sequence of activity of the different Vulcanian outbursts results clear and well described by geophysics, the underlying mechanisms of magma fragmentation operating during the different phases of the activity are still poorly understood ([Yokoo et al., 2013](#)).

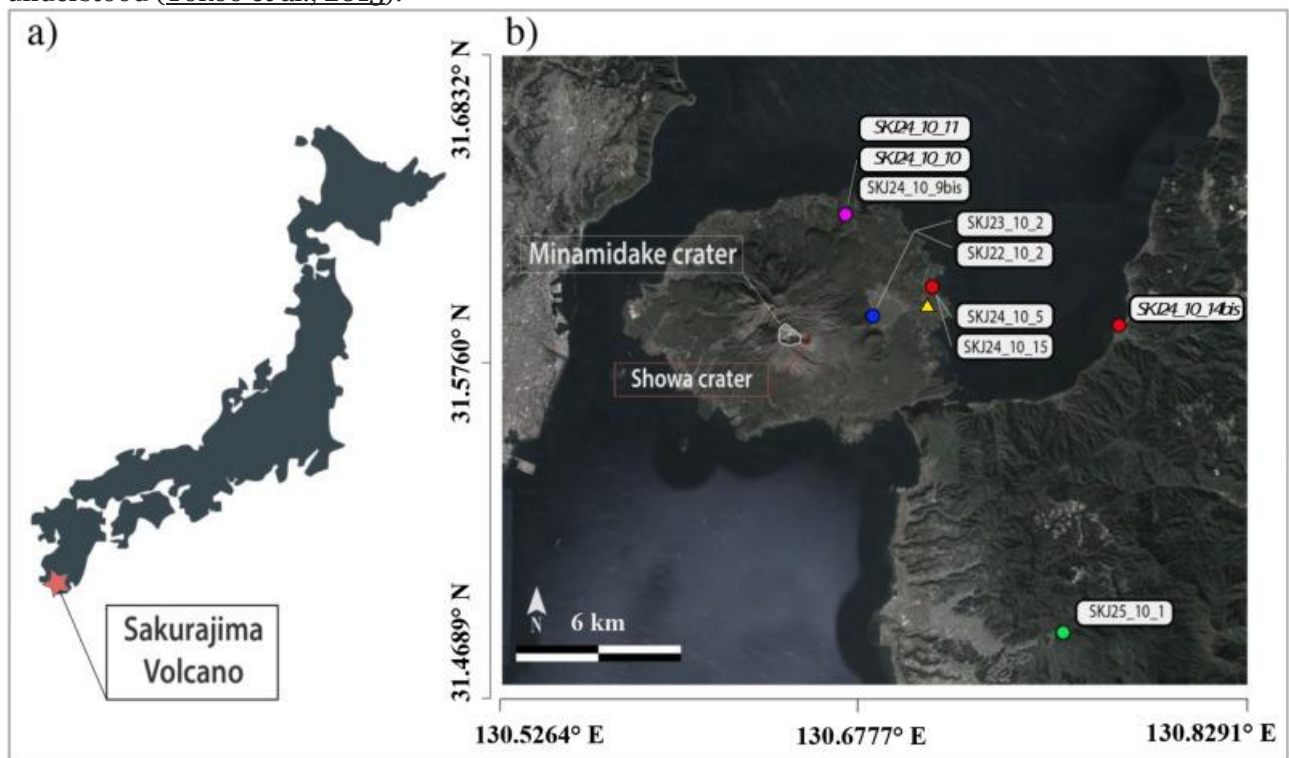


Fig. 1. (a) Location of Sakurajima volcano indicated within a sketch map of the Japan archipelago; (b) locations of the ash samples (indicated with circles) reported in the map with variable colors according to the different stages observed in the eruptive activity: Weak Ash Emission (blue circle), Vulcanian Explosion (red circles), Continuous ash venting (violet circle), and activity renewal (green circle). The yellow triangle marks the site of the thermal camera video recording (31.588974° N 130.707363° E). (For interpretation of the references to color in this figure legend, the reader is referred to the web version of this article.)

1.2. Previous studies on volcanic ash from Sakurajima activity

The first quantitative studies and descriptions of Sakurajima ash were made by [Oba et al. \(1980\)](#), who distinguished ash components based on their color identifying two types of fragments: ‘red ash’, interpreted as a mixture of hydrothermally altered and juvenile ash particles, and ‘black ash’, representing

ash produced by the disruption of the plug hosted in the vent. [Miyagi et al. \(2010\)](#) described Sakurajima ash deposits as mostly formed by juvenile, dense, glassy and blocky fragments, surrounded by planar surfaces with few large and irregular vesicles. Minor and occasional pumiceous and fluidal particles were also identified. Finally, [Miwa et al. \(2009\)](#) distinguished juvenile components from lithics based on external features like ‘smooth’ (i.e. glossy) surfaces, typical of juvenile components, and ‘non-smooth’ surfaces, interpreted as indicative of non-juvenile material. [Miwa et al. \(2013\)](#) confirmed that pumice-like and fluidal fragments are poorly present at Sakurajima, except for very large explosions. Fluidal particles collected during these events consist of glassy fragments characterized by smooth external surfaces reflecting the molten state of magma at the time of fragmentation. Conversely, the highly vesicular fragments described by [Miwa and Toramaru \(2013\)](#) show a complex external outline related to the presence of abundant, spherical vesicles (on average 40% in volume).

Based on ash features, many authors tried to relate eruptive dynamics with the processes affecting magma during ascent in the conduit. A variation in vesicularity coupled to a variation in Cl and F contents of the groundmass glass of the ash from different stages of activity, allowed [Nogami et al. \(2006\)](#) to suggest the occurrence of two distinct magma components with different volatile contents as a possible explanation of the large variability observed in the eruptive patterns. In particular, fragmentation of a more volatile-rich magma was related with an ash emission activity described as ‘Strombolian-like emission’ by [Nogami et al. \(2006\)](#), while a more degassed magma was related to activity like Vulcanian eruptions and continuous ash venting. Alternatively, [Yamanoi et al. \(2008\)](#) proposed that eruptive dynamics was controlled by the migration of vesicles within the shallower part of the conduit prior to Vulcanian explosions, resulting in a vertically layered magma column. Finally, [Miwa et al. \(2013\)](#) and [Iguchi et al. \(2013\)](#), based on ash textures and seismic signals, identified in the gradual formation of a sealing plug at the top of the system and in the repeated upward migration of magma from the shallower reservoir, two important processes controlling both the intensity and the dynamics of Vulcanian explosion at Sakurajima.

2. Analytical methods

We planned an experiment of ash collection using different observational and collection approaches in order to sample the products of a sequence of activity representative of an entire eruptive cycle: i) the phases preceding a major explosion (Phase 1); ii) the vulcanian explosion (Phase 2); iii) the restoring conditions preceding the following explosion (Phase 3).

Thermal infrared videos along the entire period of sampling were recorded with a FLIR SC660 thermal camera (3.77 Hz of frame Rate; 7.5–14 μm of spectral range; 680 \times 480 of image size; 24° \times 18° of field of view [FOV]) to follow the eruptive dynamics and to estimate plume height and ascent velocity of the eruptive mixture. Location of the camera position at the moment of the main explosion is indicated in [Fig.](#)

1. The distance of the camera from the vent was used to estimate the pixel size (in meters) of the video frames. Geometrical corrections were applied to the values of pixel size according to the inclination of the optical plane of the camera respect to the real vertical motion of the plume (section S1 of Supplementary Materials for details). Each frame was then segmented based on three customized temperature thresholds (25 °C, 75 °C and 125 °C) in order to map the regions of the plume characterized by different temperature and track their spatial evolution in time. Considering the segmented images, the coordinates of the highest pixel of the plume outline were determined for each frame of the video. This information was then used to estimate the evolution in time of the plume height and its ascent velocity, calculated as the relative difference in plume height between two contiguous frames.

A total of 8 fallout tephra samples were collected during deposition from the plume using several plastic trays of 0.33×0.39 m located under the ash fallout along the main dispersal axis at distances comprised between 2.5 and 14 km from the active vent (Fig. 1b, Fig. 2). The ash plume of each eruptive phase was visually identified and the associated deposit collected in the trays, measuring the duration of sample acquisition to estimate the average deposition rate (Fig. 2). Three deposits representative of the main Vulcanian event were collected at different distances from the vent: the first sample (SKJ24–10-5) was collected during the fallout at around 5 km from the active vent, 2 min after the onset of explosion. A second sample (SKJ24–10-14bis) was collected about 1.5 h after the explosion, approximately 11 km distant from the vent (Fig. 1b). Additionally, a third sample of selected lapilli from the Vulcanian explosion (SKJ 24–10-15) was collected over large leaves approximatively a few hundreds of meters west of SKJ 24–10-5.

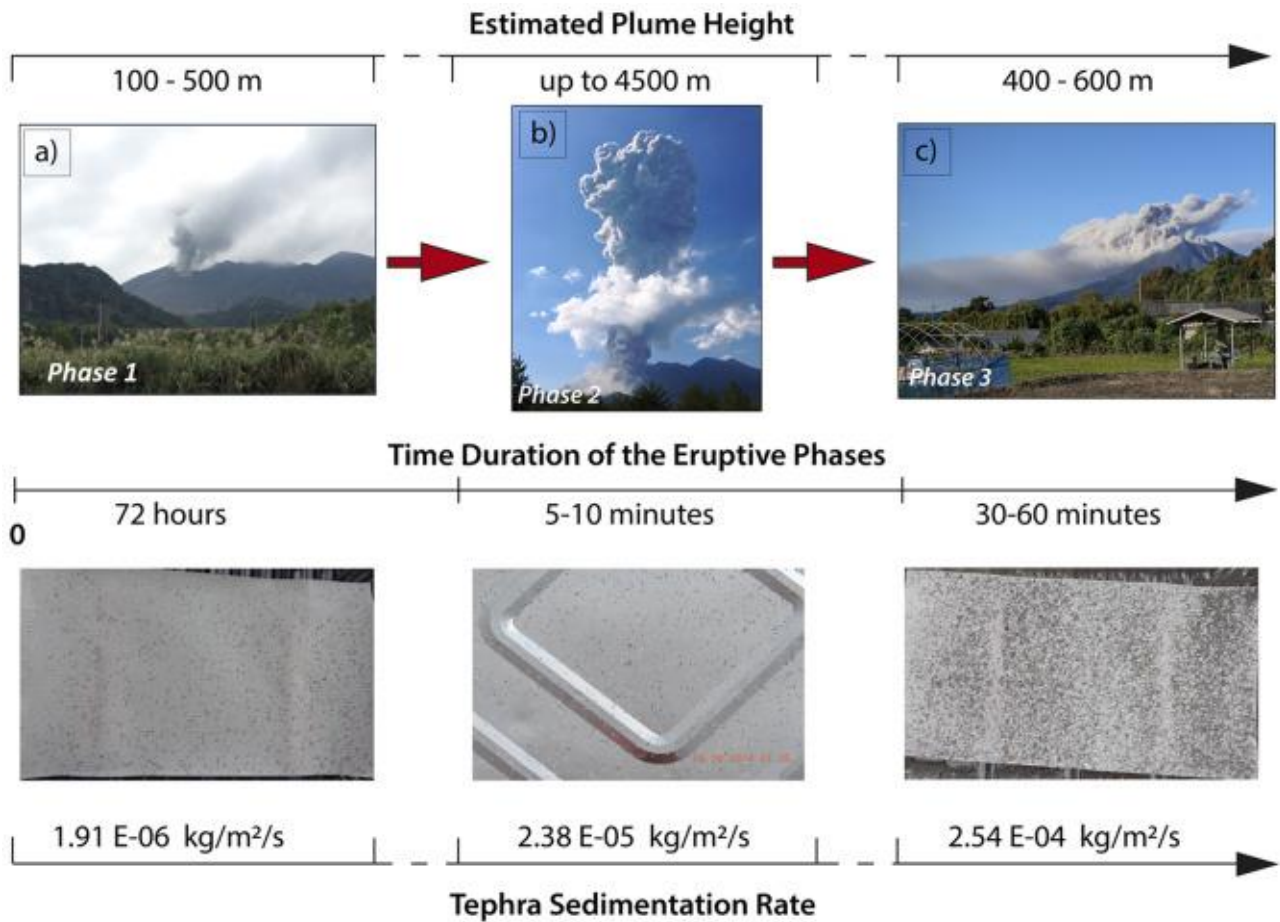


Fig. 2. a-c) The different phases shown by the eruptive cycle considered in this study: from Phase 1 (a; the beginning of the eruptive cycle) to Phase 3 (b; final step of the eruptive cycle). Important transients clearly characterize either the style and the intensity of the captured eruptive phases (a,b,c). Eruptive parameters (Temporal duration and estimated plume height) and information about tephra sedimentation (tephra sedimentation rates and images of the impact tracks left by the settling particles during fallout) associated to the different phases are also reported.

The grain-size distribution (GSD) of the ash samples was measured through a combined approach of mechanical and optical sieving. In particular, the deposit fraction coarser than 4Φ ($64 \mu\text{m}$) was sieved using the dry mechanical sieving technique, while the finer portion of the samples (particle size $<64 \mu\text{m}$) was analyzed down to $1 \mu\text{m}$ using a wet, laser-diffraction particle-size analyzer (CILAS 1180). Data from the two methods were then recombined by overlapping the two partial distributions and assuming a constant density of the ash fragments in the different deposit class sizes. Based on the presence of asymmetries and bimodality in the resulting GSDs, grain-size data were then fitted through one or two gaussian subpopulations (named SP1 and SP2) using MagicPlotStudent, a dedicated software for non-linear data fitting; the fit residuals were always efficiently minimized ($R^2 > 0.96$). The ratio between the weight % of deposit attributed to each gaussian subpopulation ($SP\text{-ratio} = wt\% SP2 / wt\% SP1$) was used to characterize each distribution together with the main statistical parameters associated to each subpopulation (Table 1).

Table 1. GPS position of the collected bulk ash samples is reported together with a set of statistical descriptors (defined according to Folk,1968) characterizing the GSDs of tephra-fallouts deposits and information upon deconvoluted subpopulations internal to the total deposits. In particular, the ‘VolFraction’ columns report also the deposit fraction (Volume %) corresponding to the coarser and, where present, the finer subpopulations (SP1 and SP2, respectively); the relative importance of these subpopulations is pointed out by the values of *SP-ratio* ($Vol(\%)SP2 / Vol(\%)SP1$).

Eruptive phase	Sample ID	Sampling location	Collection timing	Median	Mode	Sorting	Skewness	Kurtosis	Fraction SP1	MdPhi SP1
Empty Cell	Empty Cell	Empty Cell	(<i>JST</i>)	(<i>Phi</i>)	(<i>Phi</i>)	–	–	Empty Cell	(%)	(<i>Phi</i>)
Phase 1	<i>SKJ22_10_2</i>	31.586536° 130.688517°	15:30– 17:30	2.4	2.5	0.82	0.12	1.08	86	2.5
Phase 1	<i>SKJ23_10_2</i>	Ibid.	11:30– 12:35	2.4	2.5	0.77	0.15	1.20	94	2.5
Phase 2	<i>SKJ24_10_5</i>	31.5835878° 130.7001617°	12:25– 12:35	1.0	1.0	0.44	0.06	1.04	98	1.2
Phase 2 (distal sample)	<i>SKJ24_10_14bis</i>	31.574815° 130.778268°	nd	2.8	3.0	0.55	0.07	1.08	98	3.0
Phase 2 (lapilli sample)	<i>SKJ24_10_15</i>	31.5835878° 130.7001617°	–	–	–	–	–	–	–	–
Phase 3	<i>SKJ24_10_9bis</i>	31.61984° 130.6780°	12:50– 13:00	2.8	3.0	1.56	0.58	1.62	71	2.8
Phase 3	<i>SKJ24_10_10</i>	Ibid.	12:50– 13:25	2.9	3.0	1.70	0.59	1.33	65	2.9
Phase 3	<i>SKJ24_10_11</i>	Ibid.	13:25– 13:35	3.7	3.5	1.23	0.41	1.41	65	3.6
Phase 1 {new cycle}	<i>SKJ25_10_1</i>	31.4826667° 130.762016°	during the night of 25th	4.1	4.5	0.51	–0.02	1.02	100	4.3

Ash componentry was evaluated investigating the modal grain-size class (250–500 µm) through visual inspection and textural description of the grain surfaces (morphology, surface roughness, color and apparent vesicularity), distinguishing different types of juvenile or lithic material, and loose crystals. Where available, a coarser grain-size (500–710 µm) was also considered for component analysis. Analyses of external surfaces and internal groundmass textures were carried out on a randomly picked subset of around 30 juvenile particles for each deposit, using a Zeiss EVO MA15 Scanning Electron Microscope at the MEMA laboratories of the University of Florence (SEM). The shape of the particles was

quantitatively determined calculating different dimensionless shape parameters on a random 2D projected outline of the particles (APASH; [Leibbrandt and Le Pennec, 2015](#)). In each eruptive phase, the characteristic 2D shape of the different ash components that were identified was fully described for each particle type. Following [Liu et al. \(2015\)](#), we selected four dimensionless shape parameters (Circularity, Elongation, Solidity, Convexity) considered to efficiently represent all the various morphological features of the clasts. In particular, the macro-morphological features were accounted by measuring the clast Circularity (the ratio of the circular equivalent circumference to the perimeter of the particle [C_{eq}/P]) and Elongation (defined according to [Leibbrandt and Le Pennec, 2015](#) as the ratio of the particle width to the particle length [W/L]). The meso- and the micro-morphological features were instead monitored calculating respectively the clast Solidity (the ratio of the particle area to the area of the convex hull [A/A_{CH}]) and Convexity (perimeter of the convex hull to the perimeter of the particle [P_{CH}/P]), as defined in [Liu et al. \(2015\)](#).

Back-scattered electrons SEM images collected on polished sections of the same grains were analyzed to extract information on the size and content of bubbles and microlites using *Fiji*, a dedicated software for the image analysis ([Schindelin et al., 2012](#)). Bubbles and microlites, identified on the SEM images, were manually traced and segmented to measure all the primary geometrical parameters (Area, Feret diameters, Perimeter). Vesicularity was calculated as the ratio of the total surface area of the vesicles to the total analyzed cross-sectional area. In order to ensure a good representativity also for large and sparse vesicles, the vesicularity was determined using lower magnification images. The shape of the vesicles was measured directly from the images (2D cross-section), and their size was estimated as the diameter of the equivalent circle (D_{eq}).

The crystal content was computed as the total surface area of crystals to the total analyzed cross-sectional area, corrected for the area of vesicles. Information on microlite abundance was extracted using several high-magnification images for each particle, to ensure a good representativity also for the smallest classes of crystals (down to 1 μm in size).

Information on the dimension of plagioclase microlites (maximum and minimum Feret) were also used to determine the Crystal Size Distribution (CSD) for the different ash grains introducing a stereological correction using the software *CSDcorrections* (Higgins, 2000). Crystal axial ratios were derived from the CSDSlice spreadsheet ([Morgan and Jerram, 2006](#)).

Finally, an automatic image analysis of the ash grains of the different deposits was performed using a static image analysis approach with the Malvern Morphology 3GS particle analyzer. Aliquots of 13 mm^3 of ash were randomly picked from the $<355 \mu\text{m}$ fraction of each sample. During analysis, the apparent maximum projected ash shape (APASH) of a large set of ash grains (2000–3000) from each size class in the range 64–355 μm ($2 - 4\Phi$, where $\Phi = -\log_2 d$, with d being the particle diameter in mm) was automatically traced and the selected shape parameters calculated. These data were used to construct simple moving average (SMA) plots to monitor the variability of the particles shape (calculated as the

median of the sliding windows) with the size. The range of data dispersion, calculated as the first and the third quartiles, was also associated to these measures. The samples were analyzed using an appropriate set of optical magnifications (5×; 10×; 20×) in order to maintain image resolution (expressed in terms of the number of pixels entering within the 2D particle projection) as constant as possible for particles having very different size, thus avoiding scaling effects due to ‘pixellation’ of the outlines of the finer particles. The use of standard operative procedures (SOPs) allowed us to provide comparable results among different samples, since an invariant optical setting was used during all the data acquisition procedure.

3. The 22–25 October 2014 eruptive sequence

An entire Vulcanian eruptive sequence was observed at Sakurajima in the period from 22 to 25 October 2014. According to Oishi et al. (2018), to the JMA reports (<https://volcano.si.edu/volcano.cfm?vn=282080>) and based on the monthly frequency of the explosions, the rate of Sakurajima activity during October 2014 was classified as “moderate”. A total of 19 major Vulcanian explosions were recorded, each associated to ash plumes with height always below 2.5–3.5 km a.s.l.. During the whole month, the alert level of the volcano remained at 3 in a scale of 5.

Ash sampling started on 22 October, at the end of a five-days period of low-intensity activity which followed three major Vulcanian explosions occurred on 14–17 October. On 22 and 23 October the activity consisted of a low intensity ash emission (Phase 1; Fig. 2a) characterized by a very low sedimentation rate ($1.91 \times 10^{-6} \text{ kgm}^{-2} \text{ s}^{-1}$ at a distance of about 2 km from the vent) and without any associated explosive activity. After two days of weak ash emission, on 24 October at 12:05 Japanese Standard Time (JST) a strong Vulcanian explosion was recorded at Showa crater (Phase 2; Fig. 2b). The major explosion formed a strong, ash-rich plume that rapidly reached about 4.6 km a.s.l. in height and drifted E. The plume height was comparable to that of the typical major events occurring at Showa crater. This phase was characterized by a sedimentation rate of $2.38 \times 10^{-5} \text{ kgm}^{-2} \text{ s}^{-1}$ at a distance of about 5 km from the vent. The explosion was followed by a prolonged phase of intense and continuous ash emission (Phase 3; Fig. 2c), which started 2–5 min after the onset of the Vulcanian explosion and progressively decreased in intensity until vanishing after about 1 h. This activity was marked by the formation of a quasi-sustained, low-level weak plume characterized by a sedimentation rate of $2.54 \times 10^{-4} \text{ kgm}^{-2} \text{ s}^{-1}$ at about 3 km from the vent. Activity resumed around 3 h later with a continuous weak ash emission similar to Phase 1 both in intensity and in dynamics, and therefore interpreted to represent the very initial stage of a new eruptive cycle (Phase 1 {New Cycle}).

All the activity phases were recorded and described using a FLIR SC660 thermal camera, deployed at around 2 km East of the Showa crater (Fig. 1). Thermal data (Fig. 3i,l) clearly show the unsteady character of the activity during Phase 2 and Phase 3. While Phase 1 had no associated significant thermal anomaly, onset of Phase 2 was marked by the abrupt injection in the atmosphere of a hot eruptive mixture. The

plume immediately experienced a rapid acceleration, reaching the maximum vertical velocity of 220 ms^{-1} within 1 s after eruption onset (Fig. 3a-e). Within the following 8 s, the plume showed a gradual deceleration down to an ascent velocity $< 50 \text{ m/s}$, reaching by that time an elevation of about 850 m above the crater (Fig. 3b,f). At the same time, the external portion of the plume partially collapsed to feed a very small pyroclastic density current flowing over the external slope of the Showa crater with a runout of a few hundreds of meters. After 9 s from the eruption onset, the top region of the plume maintained a fairly constant and low ascent velocity with values rarely $> 30 \text{ m/s}$, before exceeding the camera field of view at around 21 s. Starting from the first few seconds after the eruption onset, the thermal anomaly associated with Phase 2 progressively decreased and completely disappeared at about 42 s (Fig. 3 c,g). However, starting from 2 min after the onset of the explosion, a persistent, although very modest in intensity, thermal signal was recorded (Fig. 3d, h) associated to the intense ash emission of Phase 3. After 20–30 min from the onset, even the thermal signal related to Phase 3 started to show a progressive decrease, completely ceasing, together with the ash emission, after about one hour.

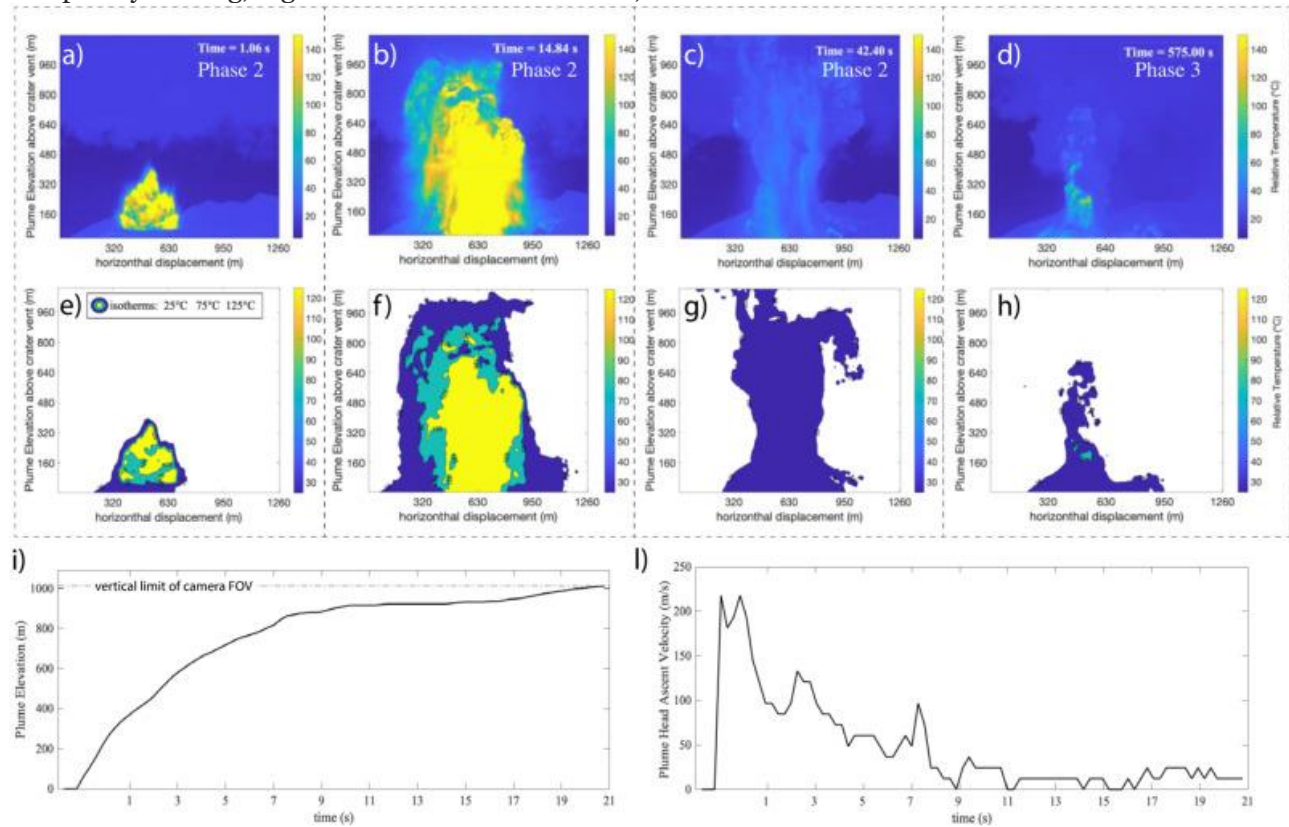


Fig. 3. Thermal footage of Phase 2 and Phase3 (a-c-e-g) taken at different timings (1.06–14.84 - 42.40 and 575.00 s) after the onset of the prominent Vulcanian explosion (Phase2). Thermal-based segmentation of the footage (b-d-f-h). Time series of plume elevation above the crater (i) and local ascent velocity of the plume head (l) derived for the first 22 s of Phase 2. Dotted line in panel l indicate the height limit of the camera Field of View (FOV).

4. Results

4.1. Grain size distribution (GSD)

The GSD of the ash samples from the different phases of activity shows significant differences in the shape (unimodal vs. bimodal) ([Fig. 4](#)) and in the corresponding parameters of skewness and sorting ([Table 1](#)). In general, the deposits belonging to the same phase of activity, collected at different times (e.g., deposits from Phase 3) or places (e.g., Phase 2) display very similar and consistent GSD ([Fig. 4](#)). Accordingly, either the $Md\Phi$ and the relative volume fraction of the two gaussian subpopulations (SP1 and SP2, coarse- and fine-grained, respectively) deconvoluted from the bulk sample show specific variations according to the activity phase ([Table 1](#)).

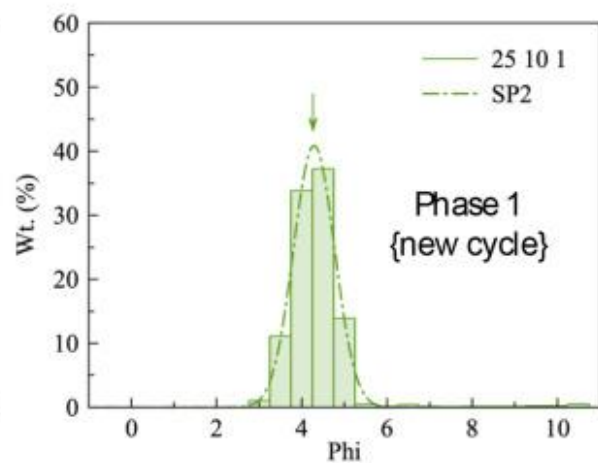
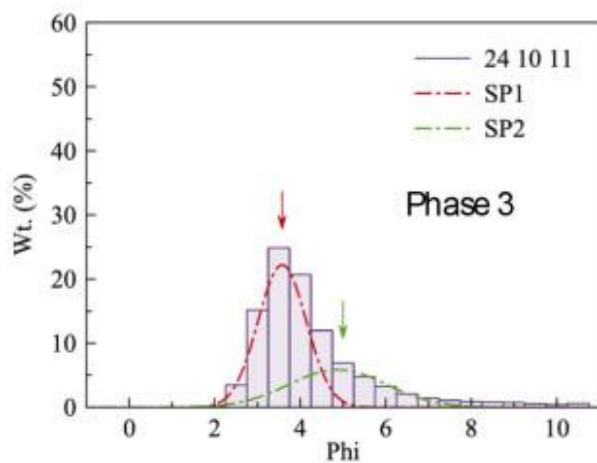
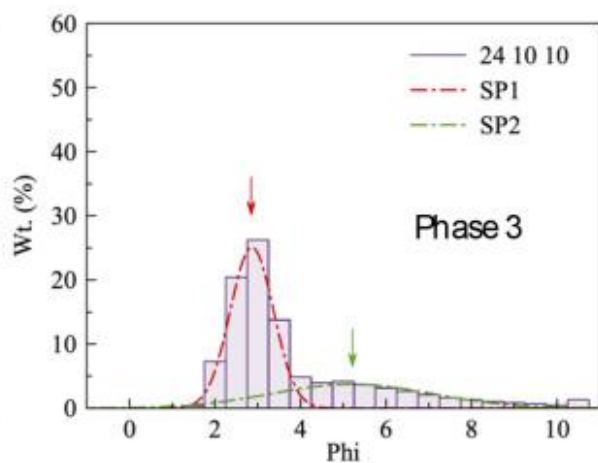
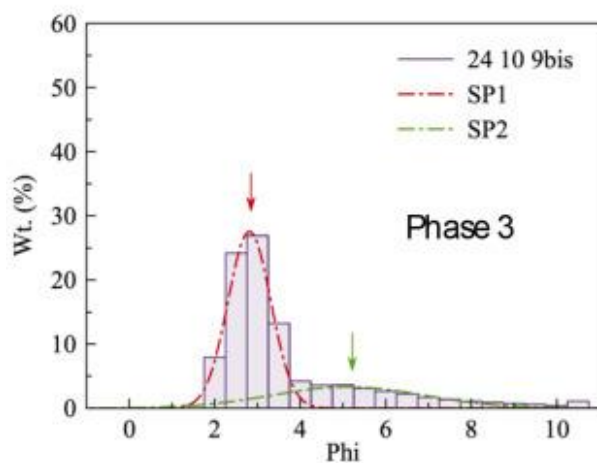
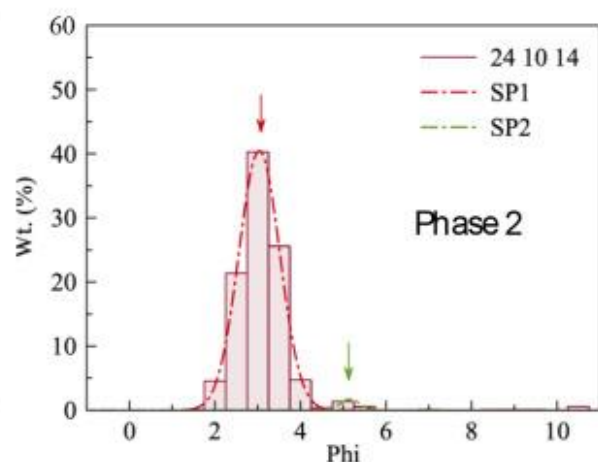
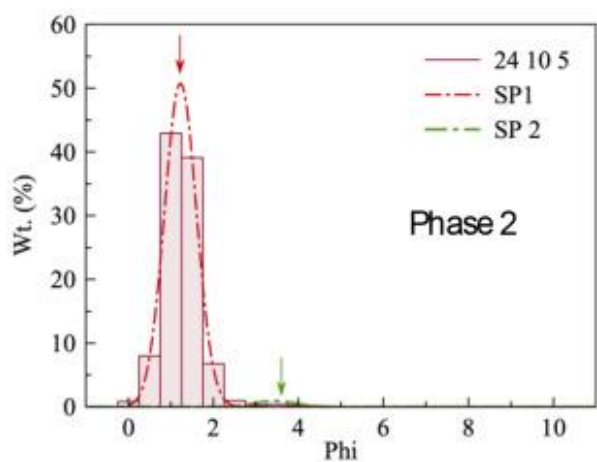
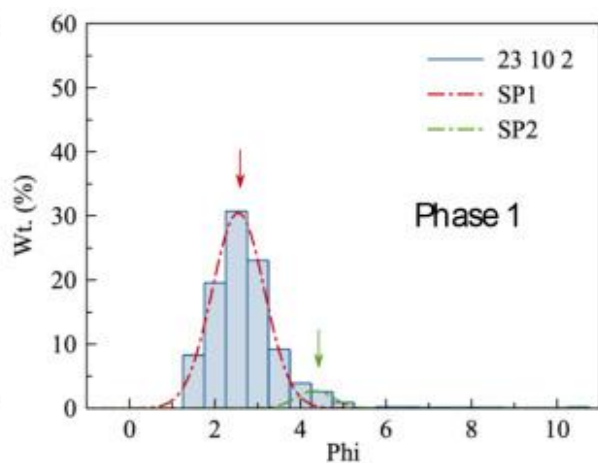
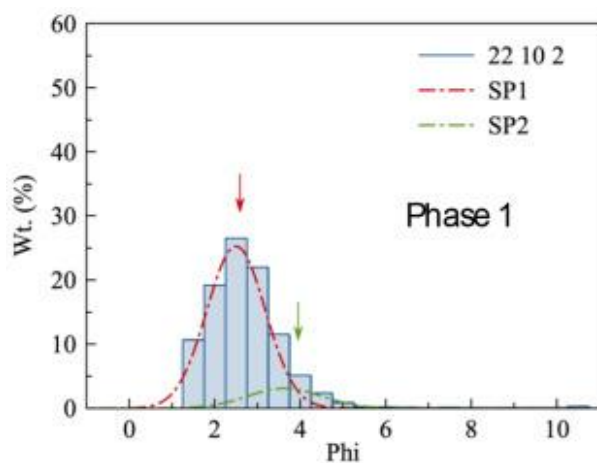


Fig. 4. Grain size distributions (GSDs) of tephra fallout samples collected during different stages of eruptive activity (color of the histograms). The internal deposit subpopulations are also represented with colored dotted lines and the position of the mean of each gaussian curve is marked by a vertical arrow (SP1 = red and SP2 = green). (For interpretation of the references to color in this figure legend, the reader is referred to the web version of this article.)

The *Weak Ash Emissions* opening the Vulcanian cycles (Phases 1) were sampled at different distances (4 km for the two samples of Phase 1; 14 for the sample of Phase 1 {New Cycle}). The GSD of the proximal samples, *SKJ22_10_2* and *SKJ23_10_2* (Table 1 and Fig. 4) clearly shows the contribution of the two SPs, with the most abundant SP1 always peaked at 2.5Φ and accounting respectively for the 86 and 94% of the total sample, and SP2 peaked at $3.6\text{--}4.3\Phi$ (Table 1). On the other hand, the distal sample of Phase 1 {New Cycle} (*SKJ25_10_1*; Table 1 and Fig. 4) is characterized by a unimodal distribution and a single population SP1 with descriptive parameters ($Md\Phi = 4.3\Phi$; $\sigma\Phi = 0.48\Phi$), very close to those of the SP2 of the other samples of Phase 1. Ash from Phase 2 clearly differs from that of all the other phases, having a nearly symmetric (Skewness = 0.06), leptokurtic (Kurtosis = 1.04) GSD, with a minor fine mode only present in the proximal sample (Fig. 4). In the GSD of sample *SKJ24_10_5* (proximal deposit: 5 km from the vent; Fig. 1b), the coarse subpopulation SP1 represents about the 98 wt% of the deposit, with an $Md\Phi$ of 1.2Φ (Table 1). SP2 has an $Md\Phi$ of around 3.5Φ and only represents the 2 wt% of deposit. The distal deposit of Phase 2 (*SKJ24_10_14*, collected 11 km far from the vent along the dispersal axis; Fig. 1b) still shows a main SP1, with $Md\Phi = 3\Phi$ and with an only minor presence of SP2, with $Md\Phi = 5.2\Phi$ (Table 1) accounting again for only the 2 vol% of the bulk GSD. The samples from Phase 3, collected at different times, are characterized by asymmetric, positively skewed distributions with a main mode between 3 and 3.5Φ (Fig. 4 and Table 1). These samples show a very pronounced fine-grained tail, with a secondary mode at around 5Φ (in two out of three samples; Fig. 4). Again, the bulk GSD can be deconvoluted ($R^2 > 0.96$) as the sum of two SPs. The finer subpopulation SP2, with an $Md\Phi$ around 5Φ , is more represented respect to the other samples, reaching about 30–35 wt% of the total (Table 1). The SP1 of these samples has an $Md\Phi$ between 2.8 and 3.6Φ (Fig. 4 and Table 1) and represents around the 65–71 wt% of the bulk deposit. Interestingly, for the three samples from Phase 3 (*SKJ24_10_9bis*; *SKJ24_10_10*; *SKJ24_10_11*) the $Md\Phi$ of SP1 records a progressive increase with time of collection (Table 1). This variation is accompanied by a decrease of the relative weight of SP1 (from 71 to 65%) and a corresponding increase in the weight of SP2, however with no visible change in its $Md\Phi$.

4.2. Characterization of the ash components

Ash deposits from the different phases are dominated by glassy, dense and blocky particles showing variably glossy external surfaces with conchoidal fractures and sharp edges, and with variable roundness. The different fragments are characterized by color ranging from intense and shiny dark grey to a translucent grey; in many cases, opaque grey colored particles were also recognized, characterized by

pitted and non-glossy external surfaces. Poorly vesicular particles, translucent, brownish to dark in color, are also a primary component, particularly in the deposits of the high intensity Phase 2. Loose, often broken crystals (i.e., plagioclase, clinopyroxene, orthopyroxene, Fe—Ti Oxides and rare olivine), are present in minor amount, together with sparse lithics, variably colored from white to yellow and brownish-red. These are generally recognized for the incipient to pervasive alteration of the fragment, and mainly derive from preexisting lava flows. Considering the very low amount of loose crystals and lithics fragments, these will be not further considered in this analysis.

Based on these general observations, three classes of ash fragments were identified ([Fig. 5](#)):

i.

Blocky Angular (BA) are formed by very poorly vesicular to dense, blocky particles with sharp edges and equant outlines, characterized by variably glossy and shiny surfaces, sometimes intercepting sparse, large and isolated vesicles (100–200 μm in diameter). These clasts commonly show external planar surfaces with typical indentation patterns, possibly resulting from the brittle fracturing of a highly viscous magma ([Fig. 5a](#)). The external surfaces are typically characterized by a sparse, small-scale roughness (generally in the order of few micrometers), mainly related to the crystallization of microlites from the groundmass glass. No evidence of magma-water interaction was revealed for these clasts after the SEM analysis (eg. surface pitting and cracking). The average values of Solidity and Convexity determined through image analysis on selected BA particles are respectively 0.930 ± 0.025 and 0.876 ± 0.022 , indicating a generally compact shape with significantly convex external outlines ([Table 2](#)). The average value of Circularity of 0.794 ± 0.040 suggests fairly regular outlines, associated to a blocky and a massive structure ([Table 2](#)). However, fragments with smoother external surfaces are also present. The most abundant groundmass microlites are represented by prismatic, sometimes acicular, euhedral and elongated (20–60 μm) microlites of plagioclase, followed by pyroxene and sparse oxide crystals. Importantly, swallowtail and skeletal morphologies of microlites are never observed among the investigated samples. A secondary population, only occasionally present within the BA clasts, is represented by sparse clusters, irregularly arranged in space, of Fe—Ti oxides crystals typically smaller than 5 μm in size. Up to 60 vol% of the groundmass is represented by residual glass. BA particles possibly correspond to the ‘*High-Crystallinity-Particles (HCP)*’ showing “*glossy surfaces*” reported by [Miwa et al. \(2013\)](#) and to the “*Black Volcanic Rocks*” (BVR) described in the study of [Kurniawan et al. \(2016\)](#).

Table 2. The ash morphometry is quantified through four a-dimensional shape parameters, according to [Liu et al. \(2015\)](#): Solidity, Convexity, Elongation, Circularity; see main text for the definition of the shape parameters. Values of apparent 2D projected ash shape of the identified ash component is provided together with its standard deviation,

for particles collected during the three eruptive phases: Blocky Angular (BA), Blocky Rounded (BR), Vesicular (VS).

Particle Type	Shape of the Identified ash components			
	Solidity	Convexity	Elongation	Circularity
Empty Cell				
BA in Phase 1	0.911 ± 0.039	0.855 ± 0.033	0.217 ± 0.099	0.771 ± 0.050
BA in Phase 2	0.941 ± 0.017	0.888 ± 0.017	0.277 ± 0.160	0.801 ± 0.037
BA in Phase 3	0.937 ± 0.020	0.886 ± 0.016	0.276 ± 0.101	0.810 ± 0.032
<i>Average</i>	0.930 ± 0.025	0.876 ± 0.022	0.257 ± 0.120	0.794 ± 0.040
BR in Phase 1	0.940 ± 0.019	0.870 ± 0.031	0.264 ± 0.128	0.799 ± 0.040
BR in Phase 2	0.960 ± 0.014	0.898 ± 0.016	0.210 ± 0.094	0.845 ± 0.025
BR in Phase 3	0.962 ± 0.011	0.898 ± 0.010	0.224 ± 0.079	0.845 ± 0.022
<i>Average</i>	0.954 ± 0.015	0.889 ± 0.019	0.233 ± 0.100	0.830 ± 0.029
VS in Phase 1	0.889 ± 0.071	0.831 ± 0.045	0.336 ± 0.186	0.736 ± 0.089
VS in Phase 2	0.930 ± 0.010	0.823 ± 0.037	0.221 ± 0.026	0.757 ± 0.036
VS in Phase 3	0.925 ± 0.026	0.861 ± 0.033	0.316 ± 0.137	0.774 ± 0.053
<i>Average</i>	0.915 ± 0.036	0.838 ± 0.038	0.291 ± 0.116	0.756 ± 0.059

ii.

Blocky Rounded (BR) are blocky, massive, poorly vesicular to dense particles generally characterized by opaque, dark to grey colors (Fig. 5b). They show average values of 0.954 ± 0.015 and 0.889 ± 0.019 for Solidity and Convexity, respectively (Table 2), suggesting largely convex shapes and rather external smooth surfaces. The average Circularity of 0.830 ± 0.029 accounts for the sub-rounded to rounded outlines, which, along with the pitted aspect of the external surfaces (Fig. 5b), make the BR particles very distinct from the BA particles. Groundmass of BR particles is characterized by the presence of two populations of microlites: the coarser-grained population (15–30 μm length) is made up of plagioclase, mafic minerals (cpx, opx, and rare olivine) and sub-euhedral Fe—Ti oxide crystals, while the finer-grained population is represented by diffuse clusters of very small ($< 5 \mu\text{m}$) Fe—Ti Oxides crystals. Differently from BA, the presence of the small Fe—Ti oxides population is pervasive in the groundmass texture (Fig. 5b), and a more diffuse μm -sized roughness affects the external surfaces. BR clasts also show the highest values of crystallization of the groundmass glass (42–45%; Table 3). Occasionally, small acicular crystals (possibly Ca-sulphates) are found on the external surfaces. BR clasts are very similar in the external aspect to those briefly described by Miwa et al. (2013) as non-juvenile particle showing ‘non-glossy’ surfaces (also corresponding to the NS-Type of Miwa et al., 2009). On the other hand, the diffuse recrystallization of the groundmass glass is strongly suggestive of

processes of intra-crater recycling of previously ejected juvenile material under high-T conditions (D'Oriano et al., 2011, D'Oriano et al., 2014; Deardorff and Cashman, 2017).

Table 3. Average microlite, vesicle and glass contents and areal MND of the ash grains in the different stages of activity. Average relative abundance of the crystal phases and vesicles are reported together with the MND calculated for the three classes of components [Blocky Angular (BA), Blocky Rounded (BR), Vesicular (VS)] considering the whole mineral assemblage. Relative abundance and MND calculated for single particles are reported in Table S2 and Table S3, in the Supplementary Material. Note that vesicularity and microlites were measured using images with different magnifications in order to ensure a good compromise between resolution and representativity.

Phase of Activity	Particle type	Tot. crystal abund.	Vesicle abund.	Oxides abund.	Mafic minerals abund.	Plagioclase abund.	Residual glass	Areal [#NumCryst/Area]	MND
Empty Cell	Empty Cell	(%)	(%)	(%)	(%)	(%)	(%)	(mm ⁻²)	
Phase 1	BA	37.1	0.6	1.2	9.5	26.4	62.4	4.4e4	
	BR	42.5	1.1	1.5	10.5	30.4	56.9	5.1e4	
	VS	35.7	21.6	1.0	8.3	26.3	58.9	2.1e4	
Phase 2	BA	41.3	1.8	1.3	9.7	30.3	57.8	2.2e4	
	BR	43.1	0.4	1.3	9.3	32.6	56.7	3.9e4	
	VS	29.4	17.9	1.0	6.9	21.5	50.5	1.9e4	
Phase 3	BA	40.3	0.8	0.8	8.4	31.1	59.3	3.4e4	
	BR	45.6	0.1	1.7	11.4	32.4	54.4	3.0e4	
	VS	36.1	11.6	1.4	8.7	26.0	63.9	3.2e4	

iii.

Vesicular (VS) clasts consist of incipiently to poorly vesicular particles (Houghton and Wilson, 1989) characterized by glossy external surfaces, translucent-brown to dark in color with external surfaces intercepting sparse vesicles, from 30 to 60 µm in size (Fig. 5c). Both Solidity and Convexity show average values that are significantly lower (0.915 ± 0.036 and 0.838 ± 0.038 , respectively; Table 2) respect to the other categories, testifying for more irregular and convoluted external outlines. Also, the Circularity of particles is significantly lower respect to other categories (0.756 ± 0.059). Vesicles are never interconnected and their abundance is largely variable, from few percent up to maximum 30 vol%. Very high values of vesicularity, typical of pumice-like material (>40–50%), have been never observed in the analyzed material, although they have been described in other eruptions (Miwa et al., 2009). The glass of VS particles is always unaltered and microlite-poor (crystal content around 30 vol%) when compared with the other two categories. Microlites are dominated by a single population, with an average size of 10–20 µm, consisting of

single prismatic, euhedral plagioclase, together with sparse mafic minerals and oxides. Importantly, the population of small Fe—Ti oxide clusters is totally absent in these clasts. VS clast can be associated to the ‘vesicular’ and ‘Low-Crystallinity-Particles (LCP)’ presented by Miwa et al. (2013), and with the “Black Vesicular Volcanic Rocks” (BVVR) of Kurniawan et al. (2016). On the other hand, they result significantly different from the *pumiceous particles* identified by Miwa et al. (2009) due to their lower and isolated vesicularity (rarely exceeding 30%).

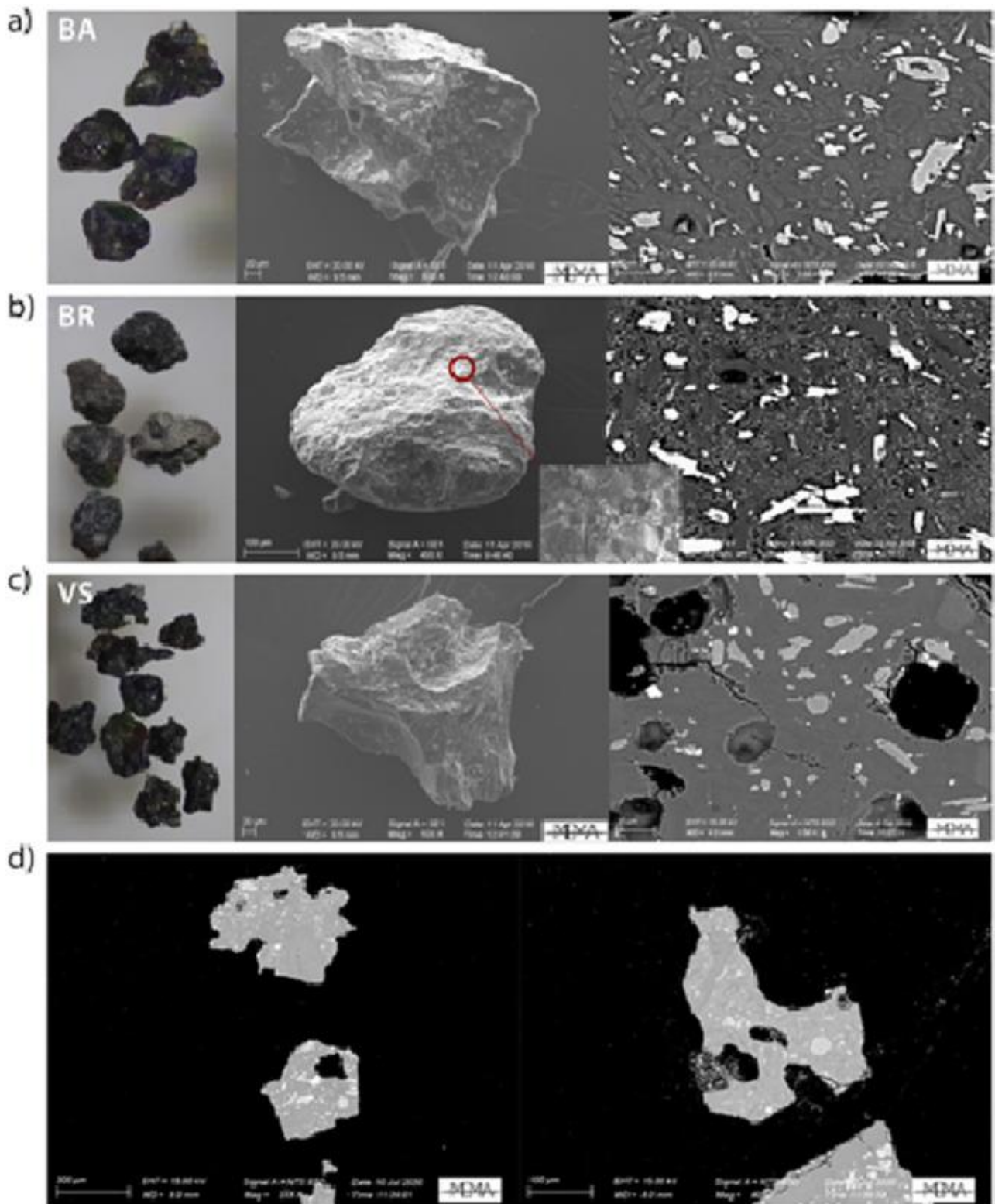


Fig. 5. Images of the identified ash components: (a) Blocky Angular (BA), (b) Blocky Rounded (BR) and (c-d) Vesicular (VS). Characteristic features of external surfaces are displayed in stereo-binocular and SE-SEM images (used in secondary electron mode), while images of the internal textures are shown in BS-SEM images (used in back scattered mode). The characteristic low vesicularity shown by the V type particles is also clearly shown in (d).

The relative proportions of the different components change during the different phases of the eruptive activity (Table 4). Ash componentry is largely dominated by BA and BR clasts. Although VS clasts represent only a minor fraction of Phase 1 products (less than 10%), they tend to significantly increase respect to BA as the eruptive sequence progresses (VS/BA ratio from 0.20 to 1.07; Table 4). An opposite trend is shown either by the BA and the BR clasts, whose relative abundances progressively decrease throughout the sequence, reaching a minimum in Phase 3 coupled to a continuous increase of VS clasts (Table 4). As a matter of facts, the dense fraction is shown to be by far dominant respect to the vesicular fraction ((BA + BR)/V) during all the phases of the eruptive sequence. Moreover, the relative proportion of BA vs. BR remains nearly constant throughout the entire sequence (Table 4).

Table 4. Relative abundance and absolute concentrations of the different ash components [Blocky Angular (BA), Blocky Rounded (BR), Vesicular (VS)] in the analyzed deposits throughout the three activity stages. Ash componentry is determined over a set of 300 randomly picked particles belonging to the modal class of the GSDs (250–500 μm).

Relative abundances			
Empty Cell	Phase 1	Phase 2	Phase 3
BR/(BA+VS)	0.53	0.39	0.24
BA/(BR + VS)	1.19	1.07	0.64
BR/BA	0.64	0.54	0.50
VS/BA	0.20	0.39	1.07
(BA+BR)/VS	8.20	3.92	1.44
Lithics/total	0.04	0.03	0.05
Cryst./total	0.04	0.09	0.22
Absolute concentrations			
	Phase 1	Phase 2	Phase 3
BA (%)	50	46	30
BR (%)	32	25	15
VS (%)	10	18	32
Lithics (%)	4	3	5
Crystals (%)	4	8	18

Finally, while the abundance of the lithic component is always very low and nearly constant, loose crystals abundance progressively increase (from 4 to 18 wt%) along the sequence (Table 4). Unfortunately, the very fine grain-size of the sample from Phase 1 {New Cycle} did not allow to estimate componentry for this stage of activity.

4.3. Quantitative characterization of ash groundmass texture

The analysis of the groundmass texture of the different clast types was addressed to characterize the relative abundance of vesicles (Table 3) and mineral phases (Fig. 6a), the areal microlite number density (MND; Table 3) of the different ash components, the shape and the crystal size distribution (CSD) of the plagioclase microlites (Fig. 6b).

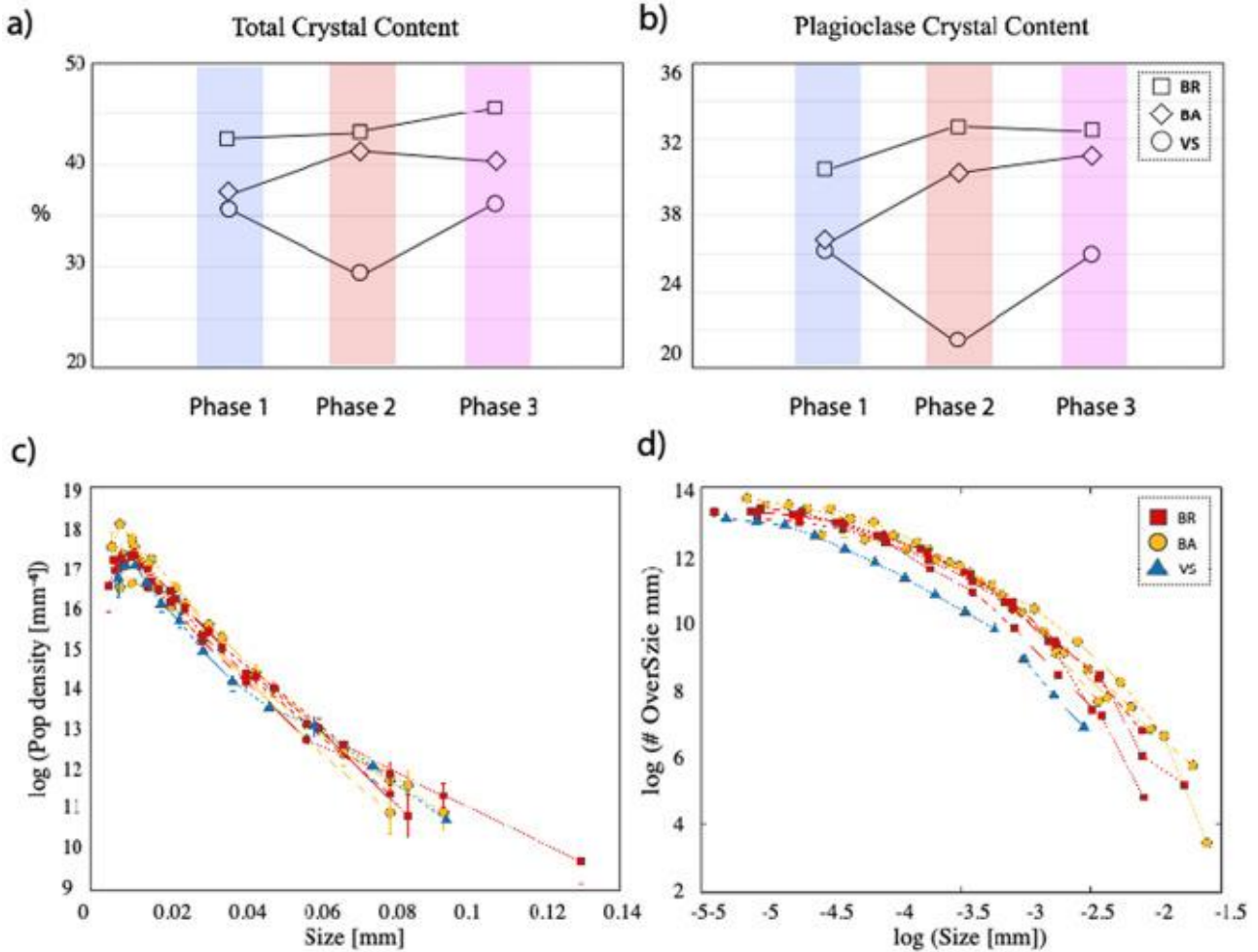


Fig. 6. a) Average microlites contents measured for the three ash components collected during different stages of activity. Variations of the total crystal contents are compared with plagioclase contents. Squares (BR), diamonds (BA) and circles (VS). Values are all corrected for the vesicle content.

(b) 3D crystal size distributions (CSDs) of plagioclase microlites for the recognized ash components (indicated by colors in the legend) selected from different phases of activity: the size is compared to the logarithm of the population density of plagioclase crystals. c) Log-log cumulative frequency distribution of the plagioclase size ' $\log(S)$ ' against the number of particles coarser than the size ' $\log(\text{#UnderSize-}S)$ '.

The average values calculated for the microlite content (Table 3) of BA and BR clasts are similar (around 40–45 vol%), being nearly constant throughout all the eruptive sequence. BR clasts have, in general, a

higher content of microlites, with the highest value (45.6 vol%) during Phase 3 (Fig. 6a, b; Table 3). VS clasts show instead a larger variability (29–36 vol%) in terms of crystal content, with a marked decrease during Phase 2 (Fig. 6a, b; Table 3). All these values agree with the crystal content reported by [Miwa et al. \(2013\)](#) respectively for HCP and LCPs ash fragments, and by [Smith et al. \(2018\)](#).

MND is calculated for all the mineral phases identified during the image analysis (Plagioclase, Mafic minerals, Oxydes). Excluding the two extreme values, MND varies by a factor of 3 (between 1.9×10^4 and $5.1 \times 10^4 \text{ mm}^{-2}$; Tables 3 and S3), in good agreement with data reported by [Kurniawan et al. \(2016\)](#).

All the CSDs calculated for plagioclase microlites display invariant linear trends for the different types of clasts, regardless of the eruptive phases (Fig. 6a, b). A single BR sample from Phase 3 (red squares in Fig. 6c) exhibits a more pronounced tail in the coarser size region (more than 100 μm). CSDs display a regression slope ($-1/G\tau$, where G is the crystal growth rate and τ is the crystallization time) variable between -77 and -109 , resulting in a dominant size of microlites, on average, around 30–40 μm ($3G\tau$; [Cashman, 1992](#); Table 5). The extrapolated nuclei number density n_0 (corresponding to the intercept of the linear regression of the CSD) is poorly variable among all the analyzed samples, with the $\ln(n_0)$ being comprised between 17.56 ± 0.06 and 18.75 ± 0.10 (Table 5). Despite the weak variability, $\ln(n_0)$ shows a clear negative relation with $3G\tau$ indicating that larger crystal sizes were related to lower nucleation rates. Importantly, the latter relation is totally unrelated with the style and timing of the activity.

Table 5. Information on the crystal size distribution (CSD) extracted for a set of ash fragments representing different phase of activity, using the software *CSDcorrections*. The microlite number density (MND) is calculated as the ratio between the number of plagioclase crystals to the analyzed area. Acronyms of ash components are defined as follow: [Blocky Angular (BA), Blocky Rounded (BR), Vesicular (VS)].

Particle ID	Phase of Activity	Particle Type	Regr. Slope ($-1/G\tau$)	Vol. Dominant size crystal ($3G\tau$)	Regression Intercept ($\ln n_0$)	Areal MND (mm^{-2})	Volumetric MND (N_v) (mm^{-3})
Empty Cell	Empty Cell	Empty Cell	Empty Cell	(mm)	(mm^{-4})	(mm^{-2})	(mm^{-3})
23 10 1	Phase 1	BA	-90 ± 3.7	0.033	18.53 ± 0.11	$9.6\text{e}3$	$6.26\text{e}5$
23 10 1	Phase 1	BR	-87 ± 4.0	0.035	18.14 ± 0.12	$7.2\text{e}3$	$5.33\text{e}5$
23 10 1	Phase 1	VS	-81 ± 3.7	0.037	17.66 ± 0.12	$5.0\text{e}3$	$3.41\text{e}5$
24 10 15	Phase 2	BA	-77 ± 1.8	0.039	17.56 ± 0.06	$5.1\text{e}3$	$3.11\text{e}5$
24 10 15	Phase 2	BR	-91 ± 1.6	0.033	18.26 ± 0.05	$6.9\text{e}3$	$4.78\text{e}5$
24 10 14bis	Phase 2	BA	-109 ± 4.0	0.028	18.75 ± 0.10	$8.1\text{e}3$	$7.29\text{e}5$
24 10 14bis	Phase 2	BR	-84 ± 3.8	0.036	17.88 ± 0.12	$5.9\text{e}3$	$4.05\text{e}5$

Particle ID	Phase Activity	of	Particle Type	Regr. Slope (-1/Gt)	Vol. crystal (3Gt)	Dominant size	Regression Intercept (lnn ₀)	Areal MND	Volumetric MND (Nv)
Empty Cell	Empty Cell		Empty Cell	Empty Cell	(mm)		(mm ⁻⁴)	(mm ⁻²)	(mm ⁻³)
24 9bis	10	Phase 3	BA	-81 ± 3.8	0.037		18.06 ± 0.12	7.3e3	4.98e5
24 9bis	10	Phase 3	BR	-77 ± 3.0	0.039		17.87 ± 0.10	7.0e3	4.20e5

All the CSD trends clearly display a turn-down of the population density for the size classes smaller than 10 µm, also present in data reported by [Miwa et al. \(2013\)](#). Typical axial ratios (short; intermediate; long) of plagioclase in the different phases are also nearly invariant (1: 3.4: 9–1: 4: 10–1: 3.4: 10, respectively for Phases 1, 2, and 3; [Table 6](#)). Again, these values are very close to those reported by [Miwa et al. \(2013\)](#) for plagioclase microlites in both LCPs and HCP fragments (1: 2.3: 9 and 1: 3.2: 10, respectively).

Table 6. Ratios of the shortest, Intermediate and Longest axis of Feldspar crystals for the three main phases of activity. The determination coefficient (R²) refers to the goodness of fit from the software ‘CSD slice’ ([Morgan and Jerram, 2006](#)).

Empty Cell	Shortest axis	Intermediate axis	Longest axis	R ²
Phase 1	1	3.4	9	0.75
Phase 2	1	4	10	0.67
Phase 3	1	3.4	10	0.75

Finally, the cumulative number frequency distributions of the plagioclase size in the bi-logarithmic space ([Fig. 6c, d](#)) display curvilinear distribution trends, suggestive of CSD not scale-invariant. All the data have a similar distribution trend, regardless of the type of ash component and the activity phase, confirming thus the very small variability already suggested by CSD plots.

4.4. Quantitative investigation of the ash shape

The variability of ash morphology along the sequence is well described by some selected shape parameters ([Cioni et al., 2014](#); [Liu et al., 2015](#); [Leibrandt and Le Pennec, 2015](#)), and by the correlation between their variability trend with the particle size. Ash from Phases 1 and 3 shows very similar trends of variation with size and, more importantly, very similar values of all the shape parameters ([Fig. 7](#)). Conversely, despite the partial overlap of the ranges of data dispersion, ash from Phase 2 displays a very distinct trend of variability respect to the other samples ([Fig. 7](#)). In general, ash from all the samples is characterized by a quite regular outline, with high Solidity and Convexity values (higher than 0.94 and 0.96, respectively), and by an elongated shape (Circularity <0.93, Elongation between 0.15 and 0.40).

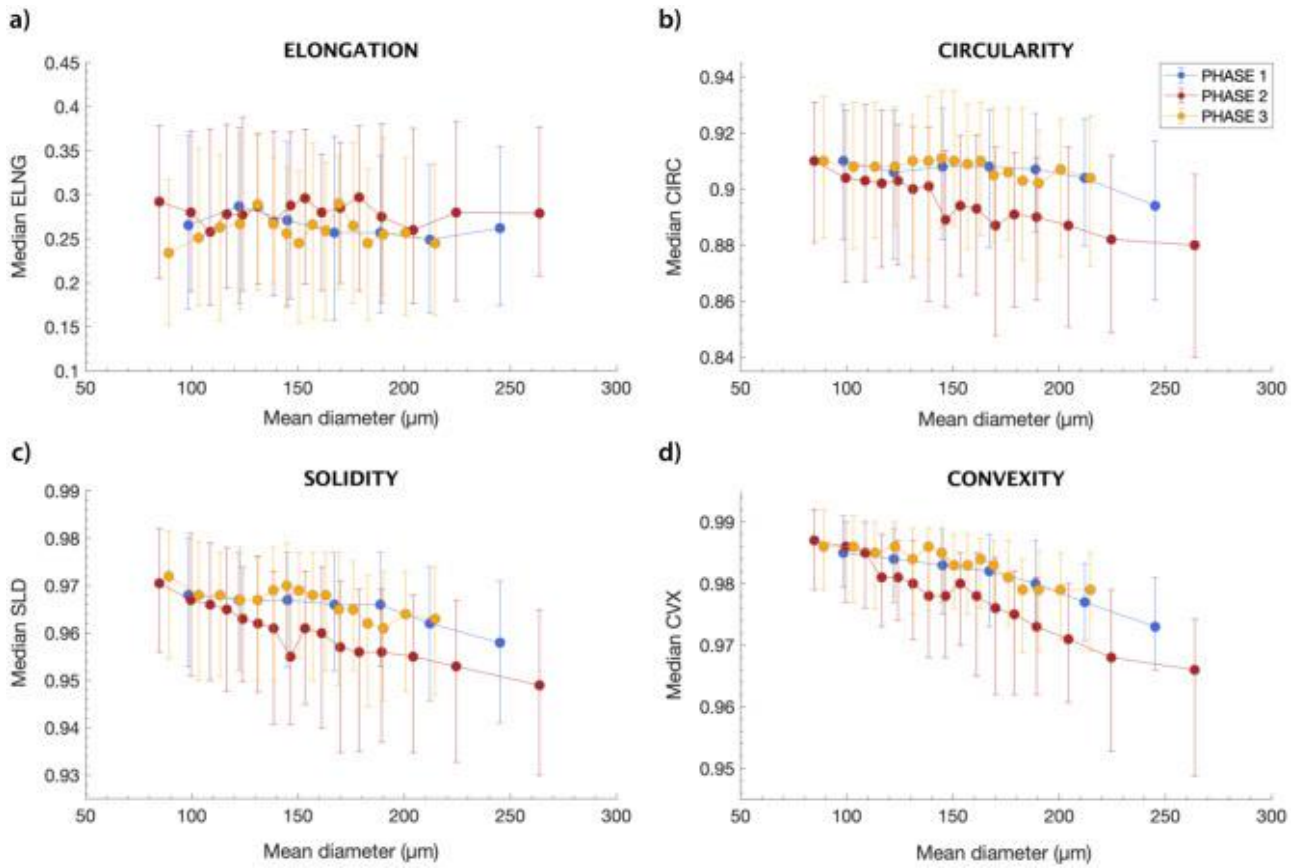


Fig. 7. The shape-versus-size trends of ash resulting from different activity styles was quantified based on four representative shape parameters (Elongation, Circularity, Solidity and Convexity). Different colors of dots in the plots refer to the identified styles of activity. Vertical bars indicate the variability (first and third quartiles) of each data window considered in the moving average plots.

As suggested by Elongation and Circularity values (Fig. 7a, b), particle shape is nearly invariant respect to the ash size for samples from Phases 1 and 3, while Circularity shows a marked, progressive increase with decreasing size for the sample from Phase 2 (Fig. 7b). On the other hand, a consistent variation of the particle shape with size is evident for Solidity and Convexity (Fig. 7c, d), suggesting the prevalence of a coarse roughness (lower values of the two parameters in the coarser particles) on the particle outline. Again, this trend is more marked for the ash of Phase 2, while ash from the other two phases has very similar values of the different parameters (Fig. 7). Importantly, the trends of Circularity, Solidity and Convexity for the ash of Phase 2 clearly diverge from the variability trends of the ash of Phase 1 and Phase 3, starting from particles size greater than 100 and 150 μm in diameter (Fig. 7). This indicates the presence of a constant size threshold for the outline roughness that characterizes ash particles from Phase 2, which is possibly coarser than about 100 μm.

5. Discussion

Ash-dominated, cyclic explosive activity represents the typical behavior of many volcanoes worldwide, which are mainly characterized by the eruption of mildly-evolved magmas. Sakurajima activity can be considered a typical case-study for such volcanoes, since it is characterized by cyclic Vulcanian eruptions with important shifts both in the intensity of the explosions and in the style of the ash emissions ([Miwa et al., 2009](#); [Iguchi et al., 2013](#); [Yokoo et al., 2013](#)). While most of the previous works on Sakurajima ash were mainly focused on the products of Vulcanian explosions (corresponding to our Phase 2), the presented dataset involves not only the products of a major explosion, but also ash from the activity preceeding and immediately following the occurrence of a the high-intensity explosion, allowing the exhaustive characterization of the different phases of a complete Vulcanian cycle. We use these data to critically discuss the main conduit and fragmentation processes involved in such cycles, and how they can be reconciled with the general knowledge about the mechanisms driving classical Vulcanian activity. Several questions are currently pending about the conduit processes that effectively control the occurrence of high-frequency Vulcanian explosions:

- What are the internal gradients of the magma plug (i.e., vesicularity, crystal contents, permeability, viscosity) and which portions of the magma conduit are directly involved in the process of ash production during the different phases of the eruptive sequence?
- Which process controls the sudden transition observed between passive ash emission and a Vulcanian explosion?
- Is fresh, volatile-rich magma coming from the deep always directly involved into the activity? Does fresh magma input represent the general trigger mechanism of Vulcanian explosions?
- What is the approximate volume of the magma conduit involved in each phase, also considering the characteristic time of plug re-generation and recharge?
- What is the variability in the intensity of explosive processes over periods much longer than a cycle?

All these questions will be addressed in the following sections, comparing our results with the numerous data existing in the literature on Sakurajima activity and discussing them in the light of a new schematic model of the processes controlling the dynamics of Sakurajima throughout a complete Vulcanian eruption cycle.

5.1. Structure of the magma conduit from morphological and textural ash features

Vulcanian activity is generally related to the fragmentation of a rigid to visco-plastic, variably crystallized and variably degassed magma plug or lava dome sealing the top of a volcanic conduit ([Clarke et al., 2002](#); [Clarke, 2013](#); [Gaunt et al., 2020](#)). The formation of evident summit lava domes has been observed to occur very sporadically at Sakurajima ([Ishihara, 1990](#)). Conversely, a variably degassed, vertically stratified magma plug is considered to be commonly present, sealing the upper portions of the conduit and generally modulating the dynamics of gas escape ([Ishihara, 1990](#); [Miwa et al., 2013](#); [Iguchi et al., 2013](#); [Yokoo et al., 2013](#); [Oláh et al., 2019](#)). Morpho-textural analysis on ash fragments efficiently informs about the variability of the internal structure of the *syn*-eruptively fragmented plug. Accordingly, the relative proportions of ash components can help to define the internal gradients of the magma conduit (e.g. [Cioni et al., 2014](#)).

The general invariance observed in the population of ash components throughout a Vulcanian cycle (i.e. constant type of components involved; [Fig. 5](#)), together with minimal time- and style-unrelated variations in the CSD of plagioclase microlites ([Fig. 6c, d](#)), possibly reflects the presence of internal gradients into the syn-eruptive magma column. This evidence also suggests a common pre-eruptive evolution for the different parcels of magma from which the ash components derive. Conversely, the total crystal content variability indicates a progressive, although slight, change of the emitted material along the eruptive cycle ([Fig. 6a, b](#)).

All the samples of the studied sequence are characterized by the common presence of three types of ash fragments ([Fig. 5](#)) displaying very distinct external shapes and internal textures. Several authors provided analyses of ash componentry on tephra products erupted during different periods of activity at Sakurajima ([Oba et al., 1980](#); [Miwa et al., 2009](#); [Miwa and Toramaru, 2013](#); [Miwa et al., 2013](#); [Kurniawan et al., 2016](#)). Regardless of the nomenclature assigned to the different ash components, we found a substantial agreement in identifying the main ash types. However, differently from what observed by [Miwa et al. \(2013\)](#) for the 2010 activity, no particles with ‘fluidal’ external morphology as well as no pumice-like particles ([Miwa and Toramaru, 2013](#); [Kurniawan et al., 2016](#)) characterized by very high vesicularity were recognized in our samples, despite the observed activity closely reflects the typical eruptive pattern and intensity of Vulcanian activity at Sakurajima (JMA on-line reports). VS clasts, in fact, represent always a minor volume fraction in all the analyzed deposits, furthermore displaying a low average vesicularity, rarely exceeding 20 vol%, which is considerably lower respect to values reported (60 vol%) for the pumiceous fragments by [Miwa and Toramaru \(2013\)](#) ([Fig. 5c, d](#)). The generally low abundance of highly-vesicular material in the studied deposits might be reconciled with the lower rates of the volcano activity (i.e. number of explosion per month) in the sampling period respect to the periods investigated by other authors, as evidenced by data reported in [Oishi et al. \(2018\)](#) (Table S4).

All the analyzed deposits are largely dominated by BA particles, characterized by high microlite contents (mostly comprised between 35 and 40 vol%), very low vesicularity (around 1 vol%), and sharp external

outlines with planar, shiny and glossy external surfaces (Fig. 5a; Table 3). As a matter of facts, all these features are typical of fragments derived from the brittle disruption of a highly viscous, semi-rigid magma portion, in agreement also with the rhyolitic composition of the residual melt determined for similar fragments by Kurniawan et al. (2016) ($\text{SiO}_2 = 74.2 \pm 1.7 \text{ wt\%}$; BVR fragments). We suggest that these clasts derive from the fragmentation of a highly degassed, highly crystallized parcel of the magma developed in the topmost portion of the plug (Fig. 8). Further elements supporting this interpretation come from the textural analysis of the ash fragments. In particular, the observed turn-down of the linear trends of CSDs for crystals smaller than $10 \mu\text{m}$ (Fig. 6c), possibly indicates the occurrence of a coarsening process typical of highly crystallized melts (Higgins, 2006). Furthermore, the euhedral and prismatic morphology of plagioclase microlites (Table 6) together with the clear evidence of a time-unrelated, negative relation between $\ln(n_0)$ and 3Gt (Table 5), likely indicate crystallization under constant and low undercooling conditions (Morgan and Jerram, 2006; Brugger and Hammer, 2010b; Shea and Hammer, 2013) experienced during prolonged stages of decompression-induced crystallization (Cassidy et al., 2015). Both these observations suggest stalling, or very slow ascent, of magma at low-pressure, that indirectly confirms the interpretation made for BA particles as derived from a highly viscous, nearly rigid magma-plug (Fig. 8).

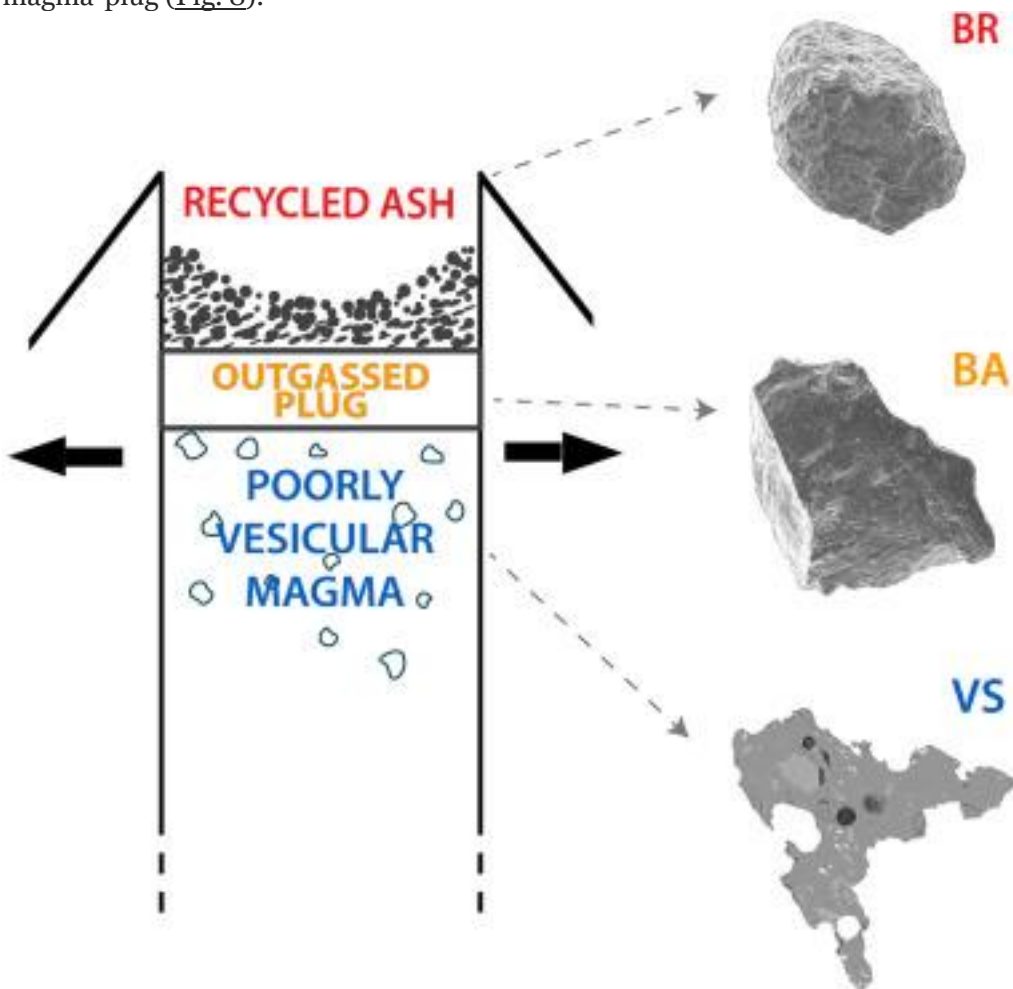


Fig. 8. Model of the vertical gradients of Sakurajima conduit inferred from analysis of ash. Three end-member clasts of the ash componentry are also presented as representative of the different conduit regions which corresponds to different depths in the magma column.

BR particles share several morphological features with BA clasts, although differing from them mainly for the lower angularity of the external outlines (Circularity: 0.830 ± 0.029 ; [Table 2](#)), the diffuse, low-scale roughness and the dull color of the external surfaces ([Fig. 5b](#)). The μm -sized population of Fe—Ti oxides overprinted on sub-euhedral microlites ([Fig. 5b](#)) is very similar to that produced during experimental re-heating of glass-bearing fragments, suggesting these clasts were modified by thermally-induced glass recrystallization during recycling in the vent area ([D'Oriano et al., 2011](#); [D'Oriano et al., 2014](#); [Deardorff and Cashman, 2017](#)). These features suggest that BR clasts invariably derive from the intra-crateric recycling of mostly BA-type particles fragmented and ejected during preceding cycles of activity ([Fig. 8](#)). This is also indirectly confirmed by the invariant groundmass textures shown by this type of fragments among all the different phases of activity, as testified for example by their constant microlite abundance and invariant CSD features ([Fig. 6c, d](#)). The gradual decrease in the relative abundance of these clasts from the initial Phase 1 to the Phase 3 ([Table 4](#)) possibly reflects the progressive clearing of the vent area due to the significant increase in the intensity of the activity, and therefore the increasing importance of the involvement of newly fragmented ash in the progressing eruptive cycle. Importantly, in previous studies BR clasts were never accurately described, as they were alternatively classified as not-vesicular, not-smooth, glassy juvenile material ([Miwa et al., 2009](#)), as lithic clasts ([Kurniawan et al., 2016](#)), or even included in the altered material ([Miwa et al., 2013](#), [Miwa et al., 2015](#)). This possibly explains our generally lower estimates of lithic fragments respect to data reported from other authors (e.g. [Kurniawan et al., 2016](#)). Lithic clasts display in fact very low relative abundances (less than few vol%) in all the analyzed deposits, in agreement with the low to moderate energy of the observed activity. This indirectly implies that an important portion (in terms of mass) of the ash involved in the eruption, although not directly produced through primary magma fragmentation, could still have a first order role in driving the convective ascent of the plume, thanks to its high temperature and abundance. The fact that BR clasts are not involved in the active fragmentation process is also in agreement with their higher abundance during periods of quasi-constant and passive ash emission ([Table 4](#)), which are indeed characterized by a very low energy of the activity ([Iguchi et al., 2008](#)). For all these reasons, we suggest that the presence of significant quantities of high-temperature, pre-fragmented and remobilized material occupying the crater area during the low energy activity phases ([Fig. 8](#)) could represent an aspect of primary importance for the definition of a general energy balance of ash production and emission at Sakurajima. We suggest this aspect could be relevant not only at Sakurajima volcano but also in similar activity contexts dominated by cyclic, low-to-mid intensity activity. For example, in the 2009–2010 activity of Tungurahua volcano “Vitreous oxidized” ash particles, representing up to 15% of the fallout deposit, were interpreted as vent-hosted and recycled materials, and their abundance throughout the

eruptive sequence is similar to that observed at Sakurajima, with a general decrease during the more energetic and vulcanian stages of the activity (Battaglia et al., 2019).

The specific characteristics that distinguish VS particles from the other types of fragments are the presence of a higher, although still modest, vesicularity (<30%) associated with a lower crystal content (Fig. 6a, b). The low vesicularity value, the rounded shape and the isolated nature of the vesicles (Fig. 5c, d) suggest a low internal permeability of this magma portion. The planar external surfaces, with no signs of fluidal deformation, and the microlite-rich groundmass, although with slightly lower MND values respect to other types ($5.0 \times 10^3 \text{ mm}^{-2}$, Table 5), still testify a rigid behavior at fragmentation for these clasts, possibly related with the rhyolitic composition of the residual melt (average $\text{SiO}_2 = 70.7 \pm 1.5 \text{ wt\%}$; BVVR fragments, Kurniawan et al., 2016). Consequently, also for VS fragments we suggest derivation from a rigid portion of the plug, possibly characterized by a slightly higher volatile content and a lower crystallinity respect to that originating the BA fragments. As a matter of facts, we suggest that the portion of magma represented by VS clasts was possibly deeper respect to that forming BA particles (Fig. 8). This part of the magma plug possibly corresponds to the region where several authors (Ishihara, 1990; Yokoo et al., 2013) identified the presence of a gas pocket suggested to be responsible for the generation of the violent pressure shock waves often recorded at the onset of the Vulcanian explosions (Fig. 8).

The presence of a magma plug with small internal gradients of vesicularity, crystal content and possibly dissolved gas is also confirmed by the poor variability of the internal texture of the different fragments (Table 5). The linear and nearly invariant CSDs (Fig. 6c) observed in all the ash fragments can be used to give constraints to the timing of cyclic plug formation. Considering a possible range of growth rates data for plagioclase crystals growing under low to intermediate undercooling conditions (10^{-8} to 10^{-9} mm/s (Cashman and Blundy, 2000; Brugger and Hammer, 2010), the crystallization time scale of the fragmented plug results in the order of around 1–10 months, thus confirming the fact that newly arrived magma is not commonly involved in the main Vulcanian explosions.

5.2. Dynamics of the recent Vulcanian activity at Sakurajima

The systematic variability revealed in the GSDs of the ash deposits, along with the sudden shifts observed in the style of the activity (Fig. 2, Fig. 3; Table 1) record important changes in the eruptive conditions, and possibly in the fragmentation mechanisms, during the observed sequence of activity at Sakurajima.

A conceptual model of the activity cycle is introduced in Fig. 9, to discuss the variability of conduit processes along the eruptive sequence. The activity preceding a Vulcanian explosion (Phase 1; Fig. 9a) is mainly characterized by a passive, low-energy degassing during which very low amounts of fine ash are only dispersed at short distances, with very low sedimentation rates ($1.91 \times 10^{-6} \text{ kgm}^{-2} \text{ s}^{-1}$ Fig. 1, Fig. 3). The absence of clear signs of transient explosive activity during this phase suggests that magma fragmentation is not driven by a large pressure accumulation within the magma plug. According to these evidences, we suggest that during Phase 1 ash dispersion is driven by the low-pressure gas release

escaping from the permeable fracture network that characterize the upper rigid portion of the outgassed plug. Under these conditions, the source of the ash conveyed in the plume possibly reflects two different mechanisms: i) the remobilization of fragmented material present in the crater infilling and produced during previous explosions (Hantusch et al., 2021), ii) clastic material produced through not-explosive, frictional fragmentation inside the fracture network in the plug (similar to fault gouges fragmentation observed in several plugs/domes elsewhere; e.g. Cashman et al., 2008) (Fig. 9a). Elutriation from an ash-filled crater (Hantusch et al., 2021) or from ash-filled fractures internal to the plug, could be a feasible mechanism for justifying the high abundance of BR type clasts in the plume. Given the average size of the fragments during this phase ($Md\Phi = 2.5\Phi = 180 \mu m$), gas ascent velocities of the order of few $m s^{-1}$ could be enough for the fluidization of these beds and elutriation of the sampled material (Tasirin and Geldart, 1999). Low ascent velocities of the gas-ash plume are also testified by the observed rapid, low-level drifting of the plume under low wind shear.

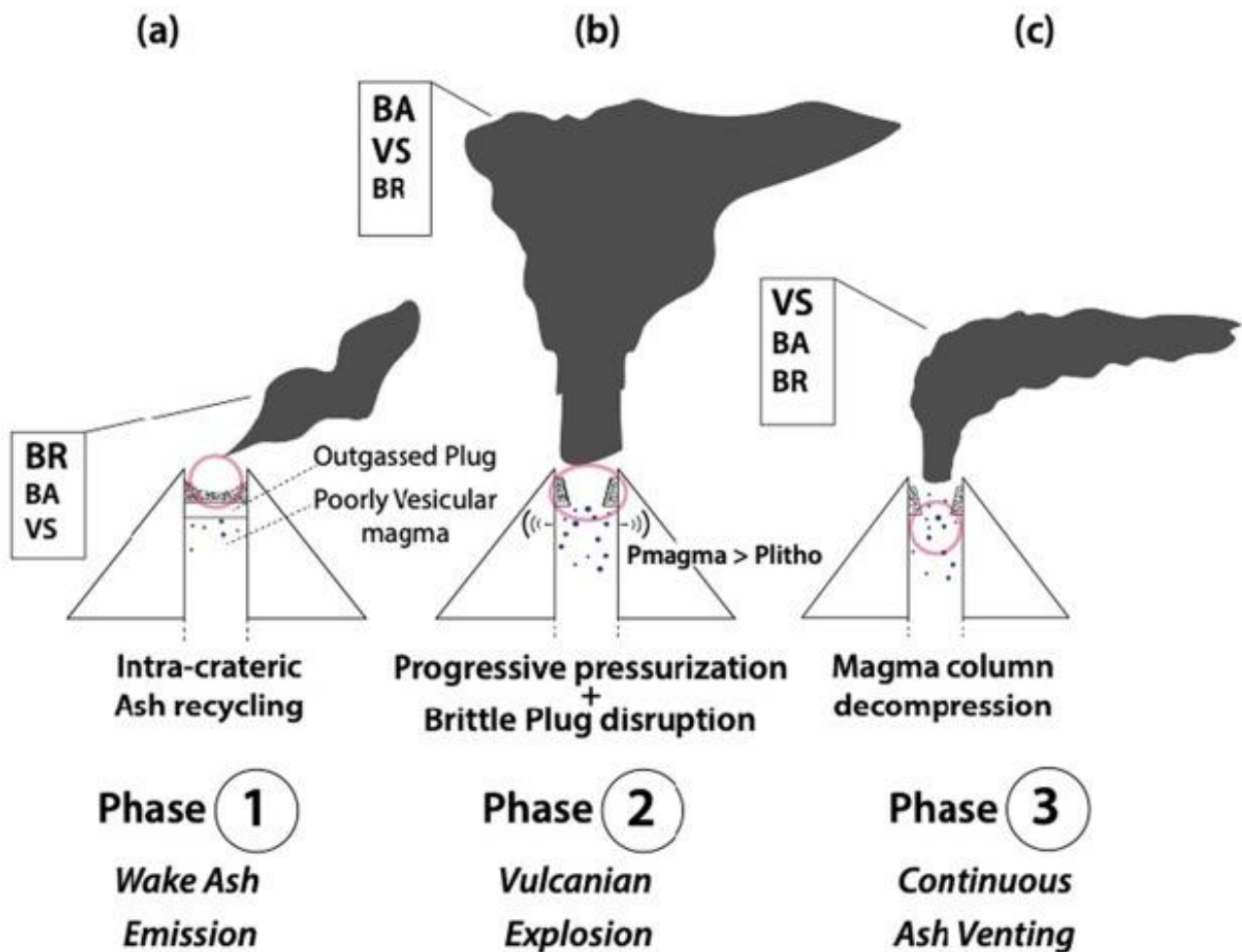


Fig. 9. Conceptual model presenting the main process controlling the eruptive dynamics of Sakurajima within the distinguished phases of activity.

Activity during Phase 2 ([Fig. 9b](#)) is represented by a short-lived, high-energy Vulcanian explosion able to eject both large ballistic blocks along the slopes of the volcano and to form a forced-thermal plume which ascended vertically up to 3–4 km height before being drifted away by the wind ([Fig. 3](#)). Shape analysis of the ejected clasts reveals that the products from this phase are clearly different from those of the other phases of the cycle ([Fig. 7](#)). A larger amount of vesicular particles (generally characterized by highly irregular contours) is present in the fine ash ejected during Phase 2, characterized by the presence of a vesicle population with a size possibly between 50 and 100 μm which mainly affects and modifies the external shape of the coarser particles. On the other hand, ash deposits are still largely populated by dense to poorly vesicular (rarely exceeding the 20%), microlite-rich particles ($\sim 30\%$). This indicates, also for the most energetic activity, the prevalence of a brittle magma fragmentation mechanism ([Fig. 9b](#)), with no or only minor participation of fresh hot magma from a deeper reservoir. The lack of fluidal or pumice-like material, often observed during other periods of Sakurajima activity, along with the substantial invariance revealed in the CSDs of plagioclase microlites and in the ash componentry, all suggest that activity was possibly fuelled by a progressive magma degassing and consequent pressure loading of the upper, partially to totally degassed portion of the magma plug occupying conduit. The short duration and the impulsive character of the explosion of Phase 2, clearly shown by thermal imagery ([Fig. 3](#)) is furthermore consistent with a rapid and abrupt release of a pressurized gas pocket. Upward gas migration and accumulation in the plug is possible due to the gradual development of a high permeability fractures network within the upper viscous portions of the plug, resulting from the high, localized internal shear of the ascending and degassing viscous magma column. This hypothesis implies to discard an important role of new magma input as an eruption trigger, and it requires a relatively slow ascending dynamics for the magma column, in order to allow a significant magma degassing and the consequent pressure loading. As a matter of facts, this agrees with the significantly lower rate of explosive activity that characterized Sakurajima in the October 2014 ([Oishi et al., 2018](#)). These considerations are also confirmed by [Yokoo et al. \(2013\)](#) who, on the basis of geophysical data, recognized as unlikely the injection of new magma from depth as the triggering process of explosions, as instead suggested by several other authors ([Iguchi et al., 2008](#); [Miwa et al., 2009](#); [Miwa and Toramaru, 2013](#)). All these data suggest that the mechanisms responsible for triggering at least part of the Vulcanian explosions at Sakurajima are mostly related to the gradual over-pressurization of the upper portions of a rigid plug (upper portions of degassing conduit) by progressive volatile exsolution from a degassing column, however without important outgassing from the plug itself ([Fig. 9b](#)). Conversely, mechanisms of pressure increase related to addition of gas-rich magma below the plug possibly control the major explosions during periods of high-rate activity (high frequency of explosions). Importantly, as already discussed for Phase 1, the large presence of recycled clasts with clear thermally-induced glass recrystallization (BR clasts) also during the Vulcanian phase can be of primary importance in determining the convective power of the resulting plume. In fact, albeit these clasts should be classified as lithic material since they were already fragmented at the moment of being engulfed

in the plume, they can still represent an important heat source for the plume development, due to their hot state and their abundance in the ejected material (up to around 50 vol%). BR clasts so assume a primary role in the total heat budget driving the plume ascent and ash dispersal at Sakurajima, and they should be distinguished from other lithic material. The high energy of the plume related to Phase 2 is well recorded by thermal analysis ([Fig. 3](#)). The coarser average grain size of the material transported in this phase (around 500 μm), considerably larger than that of the other phases, and the higher sedimentation rate ($2.38 \times 10^{-5} \text{ kgm}^{-2} \text{ s}^{-1}$; [Fig. 4](#)) are, in part, evidence of the forced thermal nature of the plume. The comparison of proximal and distal deposits ([Table 1](#)) evidences the substantial absence of an important fine-grained subpopulation (SP2) in this phase. This can be related to two concurrent processes: i) the inefficiency of ash aggregation, which would force premature ash fallout, and ii) the absence of an actively fragmentating region of high vesicularity magma. In fact, in the absence of processes like magma-water interaction, the most efficient process to produce very fine ash is the disintegration of the thin septa between the vesicles of a highly vesicular foam, not present in this phase ([Dufek et al., 2012](#)). As inferred from the visual observations of the ash deposits ([Fig. 2](#)), although ash aggregation was present it had only a minor impact in terms of mass of fine material involved in early sedimentation, just for the absence of a very fine-grained subpopulation (SP2). The high-energy, explosive fragmentation of the plug during the Phase 2 is however clearly evidenced by the concurrent abundance of both BA and VS fragments ([Table 4](#)), which suggests the involvement in the explosion of a large part of the upper portion of the plug. The contribution of vesicular ash in the *Vulcanian Explosion* (well indicated by the morphology of ash fragments in the range 50–300 μm ; [Fig. 7](#)), further confirms a more intense and deeper fragmentation of the plug during this phase. In this respect, it is interesting to note that the very low, around 0.2 wt%, water content measured by [Miwa and Toramaru \(2013\)](#) in the glass of BA-type ash with MND similar to those measured here in the October 2014 fragments, converts into a saturation pressure of only few bars ([Newman and Lowenstern, 2002](#)), corresponding to a maximum depth of around 40–50 m. Consequently, we suggest that only the very upper portion of the plug was destroyed by the explosion, according to the average mass emitted during similar explosions ([Oishi et al., 2018](#)) and to the observed upper diameter of the plug (10–20 m; [Iguchi et al., 2010](#)).

Very fine ash is instead mostly erupted during Phase 3 ([Fig. 9c](#)) of a Vulcanian cycle. This activity can be interpreted as a continued degassing phase following the partial unloading of the plug and the depressurization determined by the removal of its upper part during Phase 2 activity. In these terms, the large presence of a fine-grained (around 5 Φ) subpopulation in the ash could be the result of the sudden foaming and partial fragmentation of a slightly deeper, volatile-rich portion of the plug ([Fig. 9c](#)). The general highly crystallized groundmass texture, and especially the important increase of the free crystals recorded during Phase 3 ([Table 4](#)), clearly denote that fragmentation insisted in any case over a largely crystallized magma.

All the above considerations can be used to discuss and integrate the model proposed on the basis of geophysical observations by [Yokoo et al. \(2013\)](#) for Vulcanian activity at Showa crater. Several lines of evidence revealed by geophysics well agree in fact with the characteristics of the observed products. Firstly, the pattern of deformation preceding and accompanying Vulcanian activity from the Showa crater reveals a quite shallow source (few hundred of meters), interpreted by [Yokoo et al. \(2013\)](#) through the possible build-up and following explosive disruption of a shallow gas pocket. In this view, the fragmentation of this viscous, degassed portion of the conduit triggered a decompression wave travelling throughout the most rigid part of the plug. This well agrees with our observation of a very shallow derivation of the erupted material, with the rigid characteristics of the magma recorded in the ash texture and morphology, and with the generally small volume ejected during each explosion ([Oishi et al., 2018](#)). Similarly, evolution of deformation preceding each large eruption shows a long-term (up to several hours) inflation of the upper part of the volcano, during which the gas pocket is formed and some gas can be leaked from the upper part of the plug, possibly carrying and elutriating ash particles already present in the fracture network or in the crater area (Phase 1). Conversely, no evidence derives from our data supporting the alternative hypotheses of [Yokoo et al. \(2013\)](#) about the origin of gas accumulation as possibly related to the occurrence of repeated events of magma migration at a depth between 0 and 2 km, or of any important role of newly intruded magma in the system ([Iguchi et al., 2013](#)) during this type of activity. This aspect can be reconciled considering the low activity rates of Sakurajima during the investigated period. This could also explain the generally lower energy associated with explosions from Showa crater respect to those occurring from Minamidake crater ([Iguchi et al., 2010](#)), that often show the presence of highly vesicular, poorly crystallized, pumice-like material or of fluidal, vesicular material that we never observed in the studied sequence.

6. Conclusions

The studied eruptive sequence encompasses the whole spectrum of eruptive activities typically associated with Vulcanian eruptions at Sakurajima. These are characterized by highly energetic explosions interspersed within prolonged periods of variably intense, not-explosive ash and gas emission. We identified three different phases of activity that were all analyzed in detail: a low-energy, preparatory activity of *Weak Ash Emission* (Phase 1), preceding a main *Vulcanian Explosion* (Phase 2), then followed by a typical activity of *Continuous Ash Venting* (Phase 3). Activity renewed three hours later with a new phase of weak ash emission (Phase 1 {New Cycle}), considered to represent the very initial stage of a new cycle and prodromal to another major Vulcanian event. The study of the eruptive products of all these phases allowed us to clarify the critical role of conduit processes in controlling the mechanisms of ash formation and the eruptive dynamics of a typical Vulcanian cycle, and to critically discuss pre-existing models concerning the dynamics of Sakurajima activity.

All the analyzed deposits are largely dominated by poorly vesicular, highly crystalline particles, despite significant variability is observed both in the intensity and in the eruptive style of the activity. The morpho-textural variability of the ash suggests the presence of a significant layering and differentiation, in terms of physical properties (i.e. vesicularity and crystallinity) and magma rheology, in the magma plug occupying the volcanic conduit of Sakurajima prior and/or during the observed activity. The specific characteristics of the different ash components also suggest that a variable mechanism of magma fragmentation operated during the eruptive sequence. Based on the comparison with data reported from previous studies on Sakurajima ash, a general large-scale temporal invariance of the textural features is revealed to characterize the products of typical Vulcanian activity. The data suggest that cyclic activity of Sakurajima is mostly controlled by a quasi-static column of vertically stratified, poorly permeable, high-crystallinity magma conduit. We estimated a characteristic time-scale for the plug renewal to be around 1–10 months. Data confirm the model of [Yokoo et al. \(2013\)](#) for Sakurajima activity, in which gas accumulation in the plug, rather than the arrival of new, volatile-rich magma ([Iguchi et al., 2013](#); [Miwa et al., 2013](#)), is the most probable trigger for Vulcanian explosions during periods of “ordinary” activity. Based on this evidence we interpret the dynamics of Vulcanian eruptions at Sakurajima as controlled by the progressive pressurization of a degassed upper portion of the conduit, comprised in a range of depth between 10 and 50 m, that undergoes brittle fragmentation as the tensile strength of the viscous magma cap is reached. Finally, based on the general high-frequency of occurrence of Vulcanian explosion at Sakurajima (typically from 20 up to 400 eruption per month), and according to the long time-scale estimates provided for the plug regeneration, we suggest that also the upper cap of the magma plug is only partially removed during the Vulcanian events.

Acknowledgements

The work partially derives from the PhD Thesis of the first author. RC, GL, MP and MR acknowledge Dipartimento Protezione Civile funds to MR. Two anonymous reviewers and the Associate Editor provided constructive comments to improve a first version of the manuscript.

Authors contributions

Conceptualization: R. Cioni, P. Gabellini, N. Geshi, M. Pistolesi. Sampling: R. Cioni, P. Gabellini, N. Geshi, M. Pistolesi, T. Miwa. Thermal measurements: M. Pistolesi, G. Lacanna, M. Ripepe. Thermal data reduction: P. Gabellini. Data collection: P. Gabellini, R. Cioni. Original-draft writing: P. Gabellini. Supervision: R. Cioni. Writing-review & editing: R. Cioni, P. Gabellini, N. Geshi, M. Pistolesi, T. Miwa, G. Lacanna.

References:

- Alidibirov, M., and Dingwell, D. B. (2000). Three fragmentation mechanisms for highly viscous magma under rapid decompression. *Journal of Volcanology and Geothermal Research*, 100(1-4), 413-421.
- Battaglia, J., Hidalgo, S., Bernard, B., Steele, A., Arellano, S., & Acuña, K. (2019). Autopsy of an eruptive phase of Tungurahua volcano (Ecuador) through coupling of seismo-acoustic and SO₂ recordings with ash characteristics. *Earth and Planetary Science Letters*, 511, 223-232.
- Bernard, B., Battaglia, J., Proaño, A., Hidalgo, S., Vásquez, F., Hernandez, S., & Ruiz, M. (2016). Relationship between volcanic ash fallouts and seismic tremor: quantitative assessment of the 2015 eruptive period at Cotopaxi volcano, Ecuador. *Bulletin of Volcanology*, 78(11), 1-11.
- Bonadonna, C., Costa, A., Folch, A., and Koyaguchi, T. (2015). Tephra dispersal and sedimentation. In *The Encyclopedia of Volcanoes* (pp. 587-597). Academic Press.
- Brugger, C. R., & Hammer, J. E. (2010). Crystal size distribution analysis of plagioclase in experimentally decompressed hydrous rhyodacite magma. *Earth and Planetary Science Letters*, 300(3-4), 246-254.
- Büttner, R., Dellino, P., and Zimanowski, B. (1999). Identifying magma–water interaction from the surface features of ash particles. *Nature*, 401(6754), 688-690.
- Casadevall, T. J., and Krohn, M. D. (1995). Effects of the 1992 Crater Peak eruptions on airports and aviation operations in the United States and Canada. *US Geological Survey Bulletin*, 2139, 205-220.
- Cashman, K. V. (1992). Groundmass crystallization of Mount St. Helens dacite, 1980-1986: a tool for interpreting shallow magmatic processes. *Contributions to Mineralogy and Petrology*, 109(4), 431–449. <https://doi.org/10.1007/BF00306547>
- Cashman, K. V., and Hoblitt, R. P. (2004). Magmatic precursors to the 18 May 1980 eruption of Mount St. Helens, USA. *Geology*, 32(2), 141-144.
- Cashman, K. V., and Scheu, B. (2015). Magmatic fragmentation. In *The Encyclopedia of Volcanoes* (pp. 459-471). Academic Press.
- Cashman, K. V., Thornber, C. R., and Pallister, J. S. (2008). From dome to dust: Shallow crystallization and fragmentation of conduit magma during the 2004-2006 dome extrusion of Mount St. Helens, Washington (No. 1750-19, pp. 387-413). US Geological Survey.
- Cashman, K., and Blundy, J. (2000). Degassing and crystallization of ascending andesite and dacite. *Philosophical Transactions of the Royal Society of London. Series A: Mathematical, Physical and Engineering Sciences*, 358(1770), 1487-1513.
- Cassidy, M., Cole, P. D., Hicks, K. E., Varley, N. R., Peters, N., and Lerner, A. H. (2015). Rapid and slow: Varying magma ascent rates as a mechanism for Vulcanian explosions. *Earth and Planetary Science Letters*, 420, 73-84.

- Cioni, R., D'Oriano, C. and Bertagnini, A. (2008). Fingerprinting ash deposits of small-scale eruptions by their physical and textural features. *Journal of Volcanology and Geothermal Research*, 177(1), 277-287.
- Cioni, R., Pistolesi, M., Bertagnini, A., Bonadonna, C., Hoskuldsson, A., and Scateni, B. (2014). Insights into the dynamics and evolution of the 2010 Eyjafjallajökull summit eruption (Iceland) provided by volcanic ash textures. *Earth and Planetary Science Letters*, 394, 111-123.
- Clarke A. B., (2013) *Modeling Volcanic Processes: The Physics and Mathematics of Volcanism*, eds. Sarah AF, Tracy KPG, and Rosaly MCL. Ed Cambridge University Press. Pp (129-152).
- Clarke, A. B., Voight, B., Neri, A., & Macedonio, G. (2002b). Transient dynamics of vulcanian explosions and column collapse. *Nature*, 415(6874), 897-901.
- D'Oriano, C., Cioni, R., Bertagnini, A., Andronico, D., Cole, P.D., (2011). Dynamics of ash-dominated eruptions at Vesuvius: the post-512 AD AS1a event. *Bull Volcanol* 73, 699–715. doi:10.1007/s00445-010-0432-1.
- D'Oriano, C., Bertagnini, A., Cioni, R., Pompilio, M., (2014). Identifying recycled ash in basaltic eruptions. *Sci. Rep.* 4. doi:10.1038/srep05851
- Deardorff, N., and Cashman, K. (2017). Rapid crystallization during recycling of basaltic andesite tephra: timescales determined by reheating experiments. *Scientific reports*, 7, 46364.
- Dellino, P., and La Volpe, L. (1996). Image processing analysis in reconstructing fragmentation and transportation mechanisms of pyroclastic deposits. The case of Monte Pilato-Rocche Rosse eruptions, Lipari (Aeolian islands, Italy). *Journal of Volcanology and Geothermal Research*, 71(1), 13-29.
- Dufek, J., Manga, M., & Patel, A. (2012). Granular disruption during explosive volcanic eruptions. *Nature Geoscience*, 5(8), 561-564.
- Durant, A.J. (2015). RESEARCH FOCUS: Toward a realistic formulation of fine-ash lifetime in volcanic clouds. *Geology* 43, 271–272. <https://doi.org/10.1130/focus032015.1>.
- Fukuyama, H. (1981). Geological map of Sakurajima volcano 1: 25,000. *Geol. Map Volcanoes, Geol. Surv. Japan*, 1, 1-8.
- Gaunt, H. E., Bernard, B., Hidalgo, S., Proaño, A., Wright, H., Mothes, P., ... and Kueppers, U. (2016). Juvenile magma recognition and eruptive dynamics inferred from the analysis of ash time series: The 2015 reawakening of Cotopaxi volcano. *Journal of Volcanology and Geothermal Research*, 328, 134-146.
- Gaunt, H. E., Burgisser, A., Mothes, P. A., Browning, J., Meredith, P. G., Criollo, E., & Bernard, B. (2020). Triggering of the powerful 14 July 2013 Vulcanian explosion at Tungurahua Volcano, Ecuador. *Journal of Volcanology and Geothermal Research*, 392, 106762.
- Guffanti, M., Casadevall, T. J., and Budding K. (2010). Encounters of Aircraft with Volcanic Ash Clouds; A Compilation of Known Incidents, 1953-2009. Data Series. <https://doi.org/10.3133/ds545>.

- Hantusch, M., Lacanna, G., Ripepe, M., Montenegro, V., Valderrama, O., Farias, C., ... & Cioni, R. (2021). Low-Energy Fragmentation Dynamics at Copahue Volcano (Argentina) as Revealed by an Infrasonic Array and Ash Characteristics. *Frontiers in Earth Science*, 9, 92.
- Heiken, G., and Wohletz, K. (1985). Volcanic ash. University Presses of California, Chicago, Harvard and MIT.
- Houghton, B. F., & Wilson, C. J. N. (1989). A vesicularity index for pyroclastic deposits. *Bulletin of volcanology*, 51(6), 451-462.
- Iguchi M., Yakiwara, H., Tameguri, T., Hendrasto, M., and Hirabayashi, J. I. (2008). Mechanism of Explosive Eruption Revealed by Geophysical Observations at the Sakurajima, Suwanosejima and Semeru Volcanoes. *Journal of Volcanology and Geothermal Research* 178 (1): 1–9. <https://doi.org/10.1016/j.jvolgeores.2007.10.010>.
- Iguchi, M. (2013b). Magma Movement from the Deep to Shallow Sakurajima Volcano as Revealed by Geophysical Observations (< Special Section> Sakurajima Special Issue). *Bulletin of the Volcanological Society of Japan*, 58(1), 1-18.
- Iguchi, M., Tameguri, T., Ohta, Y., Ueki, S., and Nakao, S. (2013a). Characteristics of Volcanic Activity at Sakurajima Volcano's Showa Crater During the Period 2006 to 2011 (< Special Section> Sakurajima Special Issue). *Bulletin of the Volcanological Society of Japan*, 58(1), 115-135.
- Iguchi, M., Yokoo, A., and Tameguri, T. (2010). Intensity of volcanic explosions at Showa crater of Sakurajima volcano. *Annals of Disaster Prevention Research Institute of Kyoto University*, 53, 233-240.
- Ishihara K., (2000) Characteristics and the occurring field of vulcanian eruption. *Chikyu Monthly* 22:308–314
- Ishihara, K. (1990). Pressure sources and induced ground deformation associated with explosive eruptions at an andesitic volcano: Sakurajima volcano, Japan. Magma transport and storage.
- Ishihara, K., (1985). Dynamical Analysis of Volcanic Explosion. *Journal of Geodynamics* 3 (3): 327–49. [https://doi.org/https://doi.org/10.1016/0264-3707\(85\)90041-9](https://doi.org/https://doi.org/10.1016/0264-3707(85)90041-9).
- Jordan, S. C., Dürig, T., Cas, R. A. F., and Zimanowski, B. (2014). Processes controlling the shape of ash particles: results of statistical IPA. *Journal of volcanology and geothermal research*, 288, 19-27.
- Kamo, K., (1978). Some phenomena before the summit eruptions at Sakura-zima volcano. *Bull. Volcanol. Soc. Jpn.* 23, 53–64 (in Japanese with English abstract).
- Kamo, K., and Ishihara, K. (1989). A preliminary experiment on automated judgement of the stages of eruptive activity using tiltmeter records at Sakurajima, Japan. In *Volcanic Hazards* (pp. 585-598). Springer Berlin Heidelberg. https://doi.org/10.1007/978-3-642-73759-6_35
- Kurniawan, I. A., Sakakibara, M., and Suparka, E. (2016). Petrological Monitoring of the AD 2011–2012 Volcanic Ash from Sakurajima Volcano, Southern Kyushu, Japan. *Geosciences*, 6(1), 12.

- Leibbrandt, S., and Le Pennec, J. L., (2015). Towards fast and routine analyses of volcanic ash morphometry for eruption surveillance applications. *Journal of Volcanology and Geothermal Research* 297, 11–27. doi:10.1016/j.jvolgeores.2015.03.014.
- Liu, E.J., Cashman, K.V., Rust, A.C. (2015). Optimising shape analysis to quantify volcanic ash morphology. *GeoResJ* 8, 14–30. doi:10.1016/j.grj.2015.09.001.
- Liu, E.J., Cashman, K.V., Rust, A.C., Höskuldsson, Á. (2017). Contrasting mechanisms of magma fragmentation during coeval magmatic and hydromagmatic activity: the Hverfjall Fires fissure eruption, Iceland 1–26. doi:10.1007/s00445-017-1150-8.
- Matsumoto, A., Nakagawa, M., Aiyasaka, M., & Iguchi, M. (2013). Temporal variations of the petrological features of the juvenile materials during 2006 to 2010 from Showa Crater, Sakurajima Volcano, Kyushu, Japan. *Bull. Volcanol. Soc. Jpn.* 58, 191–212.
- Mackie, S., Cashman, K., Ricketts, H., Rust, A., & Watson, M. (Eds.). (2016). *Volcanic ash: hazard observation*. Elsevier.
- Miwa, T., & Geshi, N. (2012). Decompression rate of magma at fragmentation: Inference from broken crystals in pumice of vulcanian eruption. *Journal of Volcanology and Geothermal Research*, 227, 76-84.
- Miwa, T., & Toramaru, A. (2013). Conduit process in vulcanian eruptions at Sakurajima volcano, Japan: Inference from comparison of volcanic ash with pressure wave and seismic data. *Bulletin of Volcanology*, 75(1), 685.
- Miwa, T., Geshi, N., and Shinohara, H. (2013b). Temporal Variation in Volcanic Ash Texture during a Vulcanian Eruption at the Sakurajima Volcano, Japan. *Journal of Volcanology and Geothermal Research* 260: 80–89. <https://doi.org/10.1016/j.jvolgeores.2013.05.010>.
- Miwa, T., Shimano, T., & Nishimura, T. (2015). Characterization of the luminance and shape of ash particles at Sakurajima volcano, Japan, using CCD camera images. *Bulletin of Volcanology*, 77(1), 5.
- Miwa, T., Toramaru, A., and Iguchi, M. (2009). Correlations of volcanic ash texture with explosion earthquakes from vulcanian eruptions at Sakurajima volcano, Japan. *Journal of Volcanology and Geothermal Research*, 184(3-4), 473-486.
- Miyagi, I., Ito, J., & Shinohara, H. (2010). Re-activation process of Showa volcanic vent at Sakura jima Volcano in 2008: evidence from volcanic ash. *Bulletin of Volcanological Society of Japan*, 55, 21-39.
- Morgan, D. J., & Jerram, D. A. (2006). On estimating crystal shape for crystal size distribution analysis. *Journal of Volcanology and Geothermal Research*, 154(1-2), 1-7.
- Newman, Sally, and Jacob B. Lowenstern. "VolatileCalc: a silicate melt–H₂O–CO₂ solution model written in Visual Basic for excel." *Computers & Geosciences* 28.5 (2002): 597-604.

- Nogami, K., Iguchi, M., Ishihara, K., Hirabayashi, J. I., and Miki, D. (2006). Behavior of fluorine and chlorine in volcanic ash of Sakurajima volcano, Japan in the sequence of its eruptive activity. *Earth, planets and space*, 58(5), 595-600.
- Oba, N., Tomita, K., Yamamoto, M., Ohsako, N., and Inoue, K. (1980). Mineral and chemical composition, and mechanism of formation of volcanic ashes from Sakurajima volcano, Kyushu, Japan. *The Journal of the Japanese Association of Mineralogists, Petrologists and Economic Geologists* 75 (10): 329–36. <https://doi.org/10.2465/ganko1941.75.329>.
- Oishi, M., Nishiki, K., Geshi, N., Furukawa, R., Ishizuka, Y., Oikawa, T., ... and Miwa, T. (2018). Distribution and mass of tephra-fall deposits from volcanic eruptions of Sakurajima Volcano based on posteruption surveys. *Bulletin of Volcanology*, 80(4), 42.
- Oláh, L., Tanaka, H. K., Ohminato, T., Hamar, G., and Varga, D. (2019). Plug formation imaged beneath the active craters of Sakurajima volcano with muography. *Geophysical Research Letters*, 46(17-18), 10417-10424.
- Schindelin, J., Arganda-Carreras, I., Frise, E., Kaynig, V., Longair, M., Pietzsch, T., ... and Tinevez, J. Y. (2012). Fiji: an open-source platform for biological-image analysis. *Nature methods*, 9(7), 676-682.
- Shea, T., & Hammer, J. E. (2013). Kinetics of cooling-and decompression-induced crystallization in hydrous mafic-intermediate magmas. *Journal of Volcanology and Geothermal research*, 260, 127-145.
- Smith, C. M., Van Eaton, A. R., Charbonnier, S., McNutt, S. R., Behnke, S. A., Thomas, R. J., ... and Thompson, G. (2018). Correlating the electrification of volcanic plumes with ashfall textures at Sakurajima Volcano, Japan. *Earth and Planetary Science Letters*, 492, 47-58.
- Sparks, R. S. J., Bursik, M. I., Carey, S. N., Gilbert, J., Glaze, L. S., Sigurdsson, H., and Woods, A. W. (1997). *Volcanic plumes*. Wiley.
- Taddeucci, J., Pompilio, M., and Scarlato, P. (2004). Conduit processes during the July–August 2001 explosive activity of Mt. Etna (Italy): inferences from glass chemistry and crystal size distribution of ash particles. *Journal of Volcanology and Geothermal Research*, 137(1-3), 33-54.
- Takahashi, M., Otsuka, T., Sako, H., Kawamata, H., Yasui, M., Kanamaru, T., Otsuki, M., Kobayashi, T., Ishihara, K., & Miki, D. (2013). Temporal Variation for Magmatic Chemistry of the Sakurajima Volcano and Aira Caldera Region, Southern Kyushu, Southwest Japan since 61 ka and Its Implications for the Evolution of Magma Chamber System. *Bulletin of the volcanological Society of Japan*, 58(1), 19-42.
- Tameguri, T., Iguchi, M., and Ishihara, K. (2002). Mechanism of explosive eruptions from moment tensor analyses of explosion earthquakes at Sakurajima volcano, Japan. *Bulletin of the Volcanological Society of Japan*, 47(4), 197-215.
- Tasirin, S.M., & Geldart, D., 1999. The elutriation of fine and cohesive particles from gas fluidized beds. *Chem. Eng. Commun.* 173, 175–195. <https://doi.org/10.1080/00986449908912783>

- Wright, H. M., Cashman, K. V., Mothes, P. A., Hall, M. L., Ruiz, A. G., and Le Pennec, J. L. (2012). Estimating rates of decompression from textures of erupted ash particles produced by 1999–2006 eruptions of Tungurahua volcano, Ecuador. *Geology*, 40(7), 619-622.
- Yamanoi, Y., Takeuchi, S., Okumura, S., Nakashima, S., and Yokoyama, T. (2008). Color Measurements of Volcanic Ash Deposits from Three Different Styles of Summit Activity at Sakurajima Volcano, Japan: Conduit Processes Recorded in Color of Volcanic Ash. *Journal of Volcanology and Geothermal Research* 178 (1): 81–93.
<https://doi.org/10.1016/j.jvolgeores.2007.11.013>.
- Yokoo, A., Iguchi, M., Tamerugi, T., and Yamamoto, K. (2013). Processes Prior to Outbursts of Vulcanian Eruption at Showa Crater of Sakurajima Volcano (<Special Section> Sakurajima Special Issue). *Bulletin of the Volcanological Society of Japan*, 58(1), 163-181.